JGP Journal of General Physiology

ARTICLE

Mechanism of calcium potentiation of the α7 nicotinic acetylcholine receptor

Kathiresan Natarajan[1*], Nuriya Mukhtasimova[1*], Jeremías Corradi[4], Matías Lasala[4], Cecilia Bouzat[4], and Steven M. Sine[1,2,3a]

The α7 nicotinic acetylcholine receptor (nAChR) is among the most abundant types of nAChR in the brain, yet the ability of nerve-released ACh to activate α7 remains enigmatic. In particular, a major population of α7 resides in extra-synaptic regions where the ACh concentration is reduced, owing to dilution and enzymatic hydrolysis, yet ACh shows low potency in activating α7. Using high-resolution single-channel recording techniques, we show that extracellular calcium is a powerful potentiator of α7 activated by low concentrations of ACh. Potentiation manifests as robust increases in the frequency of channel opening and the average duration of the openings. Molecular dynamics simulations reveal that calcium binds to the periphery of the five ligand binding sites and is framed by a pair of anionic residues from the principal and complementary faces of each site. Mutation of residues identified by simulation prevents calcium from potentiating ACh-elicited channel opening. An anionic residue is conserved at each of the identified positions in all vertebrate species of α7. Thus, calcium associates with a novel structural motif on α7 and is an obligate cofactor in regions of limited ACh concentration.

Introduction

The α7 nicotinic acetylcholine receptor (nAChR) was initially discovered as a high affinity α-bungarotoxin–binding protein in the brain (Bosmann, 1972) and cultured neurons (Greene et al., 1973). Subsequent cloning (Schoepfer et al., 1990) and biochemical analyses (Drisdel and Green, 2000) showed that α7 is a pentamer composed of five identical subunits. α7 is among the most abundant types of nicotinic receptors in the brain and lodges within the plasma membranes of neurons (Bosmann, 1972), astrocytes (Sharma and Vijayaraghavan, 2001), and microglia (Shytle et al., 2004). Although α7 is found in many regions of the brain, it is enriched in the hippocampus, cerebral cortex, basal ganglia, and cerebellum (Breese et al., 1997). α7 is also present in the periphery (Broide et al., 2019), including the autonomic ganglia and neuroendocrine, gastrointestinal, lung, and lymphoid tissues (Cuevas et al., 2000; Wang et al., 2003; Plummer et al., 2005). The ion channel of α7 is highly permeable to calcium (Fucile, 2004), on par with that of the NMDA receptor (Séguéla et al., 1993); thus, in addition to mediating excitation, α7 can couple to calcium-dependent intracellular second messengers. α7 contributes to cognition (Leiser et al., 2009), sensory processing (Alkondon et al., 2000), attention (Williams et al., 2012), working memory (Yang et al., 2013), and reward (Mansvelder and McGehee, 2000) and is an emerging therapeutic target for neurodegenerative, neurological, and psychiatric disorders (Dineley et al., 2015; Deutsch et al., 2016).

In the brain and many peripheral tissues, cholinergic nerve terminals contact postsynaptic regions largely devoid of densities associated with point-to-point synaptic transmission (Descarries et al., 1997; Lendvai and Vizi, 2008). In addition, a major population of α7 localizes distant from cholinergic nerve terminals and postsynaptic densities (Jacob and Berg, 1983; Jones and Wonnacott, 2004; Duffy et al., 2009). Thus, an important mechanism for α7 signaling is volume transmission, where cholinergic stimulation elicits a temporally and spatially graded response that changes in concert with overall cholinergic tone (Sarter et al., 2009). In volume transmission, nerve-released ACh diffuses a relatively long distance before reaching its receptor target, and as a consequence, dilution and enzymatic hydrolysis reduce the ACh concentration available to occupy receptor binding sites. The low potency of ACh in activating α7 (median effective concentration [EC_{50}], ∼100 µM; Eiselé et al., 1993; Andersen, et al., 2013) suggests that in regions distant from sites of ACh release, only a small proportion of the receptor's five binding sites will be occupied. However,

[1]Receptor Biology Laboratory, Department of Physiology and Biomedical Engineering, Mayo Clinic College of Medicine, Rochester, MN; [2]Department of Molecular Pharmacology and Experimental Therapeutics, Mayo Clinic College of Medicine, Rochester, MN; [3]Department of Neurology, Mayo Clinic College of Medicine, Rochester, MN; [4]Instituto de Investigaciones Bioquímicas, Departamento de Biologia, Bioquimica y Farmacia, Universidad Nacional del Sur–Consejo Nacional de Investigaciones Científicas y Técnicas, Bahía Blanca, Argentina.

*K. Natarajan and N. Mukhtasimova contributed equally to this paper; Correspondence to Steven M. Sine: sine.steven@mayo.edu.

extracellular calcium potentiates nAChRs from a variety of neurons (Vernino, et al., 1992; Mulle, et al., 1992; Amador and Dani, 1995), as well as α7 expressed in heterologous systems (Eiselé et al., 1993). Thus, in regions remote from sites of ACh release, extracellular calcium could act as an allosteric modulator of α7.

Although homeostatic processes maintain the extracellular calcium concentration at ∼2 mM, computational studies show that in extracellular regions with small volume, such as the neuropil, the local calcium concentration can change transiently and over a physiologically significant range (Egelman and Montague, 1999). Measurements of extracellular calcium concentration in the brain confirm that neuronal stimulation transiently depletes extracellular calcium (Nicholson, et al., 1977; Rusakov and Fine, 2003). In pathological conditions, such as epileptic seizures, hypoxia, or ischemia, extracellular calcium concentrations fluctuate (Pumain et al., 1983; Silver and Erecińska, 1990). Thus, within small extracellular volumes, activity-dependent changes in extracellular calcium concentration could modulate α7 signaling.

Despite the physiological significance of calcium potentiation of α7, the biophysical and structural mechanisms behind potentiation have not been fully elucidated. In a seminal study using a receptor chimera composed of α7 sequence in the extracellular domain and 5-HT3 receptor sequence in the transmembrane and intracellular domains (Galzi, et al., 1996), mutation of several negatively charged residues near the site of agonist binding altered or prevented calcium potentiation of ACh-elicited macroscopic currents. In a second study using full-length α7 with a pore mutation that enhanced agonist sensitivity (McLaughlin et al., 2006), covalent cross-linking of β-strands flanking the ligand binding site endowed barium with agonist-like activity. Activation by barium was blocked with the α7-selective competitive antagonist MLA and was eliminated by mutation of a negatively charged residue identified in the study of the chimeric α7/5-HT3 receptor. Although these studies provided important insights into calcium potentiation of α7, how calcium potentiation manifests at the level of single receptor channels and how calcium interacts with the receptor at the atomic scale remained unresolved.

To define biophysical counterparts of calcium potentiation of the α7 nAChR, we recorded single-channel and macroscopic currents through human α7 nAChRs expressed in mammalian fibroblasts. To identify structural counterparts of calcium potentiation, we conducted MD simulations using the x-ray structure of a pentameric α7-like ligand binding domain (Li et al., 2011) in the presence of calcium ions. We then mutated candidate residues identified by simulation within the full-length human α7 nAChR and recorded single-channel and macroscopic currents to identify sites required for calcium potentiation.

Materials and methods

Expression and mutagenesis of the human α7 nAChR

BOSC-23 cells, a cell line derived from HEK 293 cells (Pear et al., 1993), were maintained at 37°C in Dulbecco's modified Eagle's medium supplemented with 10% FBS until they reached ∼50% confluence. Thereafter, cDNAs encoding wild-type or mutant human α7 nAChRs, the chaperone NACHO, and GFP were co-transfected by calcium phosphate precipitation; the ratio of α7 to NACHO cDNAs was 1:4. GFP was included to allow identification of transfected cells for patch-clamp recording. The cDNA encoding NACHO was synthesized by GenScript and then subcloned into the mammalian expression vector pRBG4 (Lee et al., 1991) and was required for expression of the α7 nAChR on the cell surface (Gu et al., 2016). The mutations E185Q, E158A, and D160S were generated using the QuikChange site-directed mutagenesis kit (Agilent Technologies) and were confirmed by sequencing the entire coding region. Patch-clamp recordings were made 24–48 h following transfection.

Single-channel recordings from cell-attached patches

Single-channel currents were recorded in the cell-attached patch configuration with a membrane potential of −100 mV and a temperature of 21°C. Patch pipettes were fabricated from type 8250 glass (King Precision Glass), coated with Sylgard 184 (Dow Corning), and heat polished to yield resistances of 5–8 MΩ. For recordings without calcium, the extracellular and pipette solutions contained (in mM) 142 KCl, 5.4 NaCl, 1 EGTA, and 10 HEPES, adjusted to pH 7.4 with NaOH. For recordings with either calcium or barium, the extracellular and pipette solutions contained (in mM) 142 KCl, 5.4 NaCl, 1.7 $MgCl_2$, either 1.8 $CaCl_2$ or 1.8 $BaCl_2$, and 10 HEPES, adjusted to pH 7.4 with NaOH. ACh, at a concentration of 100 mM in dH_2O, was stored at −80°C, and dilutions to the final concentrations were made on the day of each experiment.

Methods for data acquisition and event detection were as described (Mukhtasimova et al., 2016). Briefly, single-channel currents were recorded using an Axopatch 200B patch-clamp amplifier, with the gain set to 100 mV/pA and the internal Bessel filter to 100 kHz. Data were sampled at intervals of 0.2 μs using a National Instruments model BNC-2090 A/D converter with a PCI 6111e acquisition card and recorded to the hard disk of a PC computer using the program Acquire (Bruxton Corporation). Data were accepted for analysis if the RMSD of the baseline noise was between 120 and 180 fA at 5 kHz bandwidth. Traces of single-channel currents were digitally filtered at 25 kHz, and channel openings and closings were detected using the half-amplitude threshold criterion using the program TAC4.2.0 (Bruxton Corporation). Overlapping channel openings, although rare due to the inherently brief mean open time, were excluded from analysis. Dwell time histograms were plotted using a logarithmic abscissa and a square root ordinate (Sigworth and Sine, 1987) with a uniformly imposed dead time of 8 μs and were fitted by the sum of exponentials by maximum likelihood using the program TACFit 4.2.0. Statistical analyses of the frequency of channel opening and the average duration of channel openings were performed using an unpaired nonparametric Mann-Whitney test within GraphPad Prism version 5.04.

Single-channel recordings from cell-free outside-out patches

Following formation of a giga-ohm seal, the membrane beneath the patch pipette was ruptured, and the pipette was slowly pulled away from the cell until a cell-free outside-out patch

formed (Hamill et al., 1981). The solution within the pipette contained (in mM) 134 KCl, 10 HEPES, 5 EGTA, and 1 $MgCl_2$. The external solution with calcium contained 150 NaCl, 10 HEPES, 1.8 $CaCl_2$, and 1.0 $MgCl_2$. The external solution without calcium contained 150 NaCl, 10 HEPES, and 1.0 $MgCl_2$. Single-channel currents were recorded with a membrane potential of −70 mV. The tip of the patch was perfused with external solution containing 10 µM ACh with calcium for 30 s, followed by 30 s without calcium, using a system composed of elevated solution reservoirs for gravity-driven flow and switching valves controlled by a VC3 controller (ALA Scientific; Liu and Dilger, 1991; Corradi et al., 2009). The solution exchange time was estimated by the change in the open pipette resistance upon switching between solutions with different osmolarity and ranged between 0.1 and 1 ms. Single-channel currents were digitized at 5 µs intervals using an Axopatch 200B patch-clamp amplifier (Molecular Devices). Single-channel events were idealized by the half-amplitude threshold criterion using the segmental k-means procedure within QuB 2.0.0.28 software (Qin et al., 1996), with a low pass digital filter of 7 kHz and a dead time of 30 µs.

Macroscopic current recordings

Macroscopic currents were recorded in the whole-cell configuration at a holding potential of −50 mV. External solution containing ACh with or without calcium was applied in pulses of 1.5-s duration, interspersed by a 10-s recovery application of external solution with calcium. Macroscopic currents were acquired using the program WinWCP V5.3.7 (Strathclyde Institute of Pharmacy & Biomedical Sciences), filtered at 5 kHz, digitized at 20 kHz, and analyzed using Clampfit 10.4 (Molecular Devices). Currents in response to three to five applications to the same cell were recorded for each condition, and the values obtained from different cells were averaged.

MD simulations

All-atom MD simulations were conducted using the x-ray structure of the ligand-binding domain of an α7/AChBP chimera (Li et al., 2011) in the presence or absence of calcium ions. The coordinates for the α7/AChBP chimera were downloaded from the Protein Data Bank (PDB accession no. 3SQ9). 30 Ca^{2+} ions and counter anions were placed randomly around the protein, and the system was placed in a cubic box 120 Å in each dimension and solvated with TIP3P water molecules and 150 mM NaCl. Ca^{2+} ions were modeled using the CHARMM36m force field. All MD simulations were performed under periodic boundary conditions using the NAMD software package (Phillips et al., 2005) with the CHARMM36m force field, and the particle-mesh Ewald sum method (Essmann et al. 1995) was used to treat long-range electrostatic interactions. The CHARMM36m force field provides improved accuracy in generating backbone conformational ensembles (Huang et al., 2017). All the bond lengths involving hydrogen atoms were fixed using the SHAKE algorithm (Ryckaert et al., 1997), allowing for an integration time step of 2 fs. A 12-Å cutoff was used for nonbonded van der Waals interactions. First, the system was energy minimized over a maximum of 10,000 steps using the steepest descent energy minimization algorithm. Next, the system was equilibrated in the constant number, volume, and temperature ensemble for up to 5 ns, and finally production MD runs of 100 ns for the calcium-free system and 150 ns for the calcium-added system were performed in the constant number, pressure, and temperature ensemble. Coordinates for the trajectory were saved every 10 ps.

Residues within wild-type α7/AChBP (PDB accession no. 3SQ9) that were predicted to form calcium binding sites were mutated (E158A, D160S, and E185Q) in silico using the mutagenesis wizard in Pymol (DeLano, 2002). For each mutant, the system was energy minimized, equilibrated, and simulated up to 100 ns following the above-mentioned protocol for the simulations of wild-type α7/AChBP. From the endpoint of the calcium-free simulation for each mutant, the protein conformation was taken, and 30 Ca^{2+} ions, with charge neutralizing anions, were placed randomly around the protein; the system was equilibrated, and production simulations up to 100 ns for E185Q and D160S and 150 ns for E158A were performed using the same protocol described above to assess calcium association with wild-type α7/AChBP.

Electrostatic analysis

The electrostatic surface potentials of wild-type and mutant α7/AChBP were calculated using the PDB2PQR (Dolinsky et al., 2007) and the Adaptive Poisson-Boltzmann Solver (APBS; Baker et al., 2001) plugins in Pymol. APBS software solves the equations of continuum electrostatics for the macromolecules. The use of continuum solvation methods by APBS software utilizes complete structural data and force field parameters such as atomic charges and atomic radii, which are obtained through the PDB2PQR software. The electrostatic potential is computed by solving the Poisson-Boltzmann equation:

$$\nabla.\varepsilon(r)\nabla\phi(r) - \kappa\phi(r) = -4\pi\rho(r),$$

where $\varepsilon(r)$ is the position-specific dielectric constant, $\phi(r)$ is the position-specific electrostatic potential, κ is the reciprocal of the Debye length, and $\rho(r)$ is the position-specific charge density.

RMSD analysis

To compare the overall structural changes during the calcium-free and calcium-bound simulations, the RMSD for all atoms in the protein was calculated. RMSD values were calculated for each frame along the entire trajectory as a function of time with respect to the starting structure for both the calcium-free and calcium-bound simulations. The RMSD of atoms within a molecule with respect to a reference structure, r^{ref}, is calculated as:

$$RMSD = \left[\frac{1}{M}\sum_{i=1}^{N} m_i \left|r_i(t) - r_i^{ref}\right|^2\right]^{\frac{1}{2}},$$

where $M = \sum_i m_i$, m_i is the mass of atom i, and $r_i(t)$ is the position of atom i at time t after least squares fitting of the trajectory snapshots to the reference structure.

Radius of gyration (R_g) analysis

The R_g was calculated to detect changes in the compactness of the protein during MD simulations in either the presence or

absence of calcium. The R_g is defined as the distribution of the atoms of a protein around an axis through its center of mass. It is used to identify various polymer shapes of a protein and predict structural changes. The R_g is calculated according to:

$$R_g = \left(\frac{\sum_i |r_i|^2 m_i}{\sum_i m_i} \right)^2,$$

where R_g is the radius of gyration, m_i, is the mass of atom i, and r_i is the position of atom i with respect to the center of mass of the molecule.

Online supplemental material

Fig. S1 shows the time evolution of interatomic distances between the associating calcium ion and the oxygen atoms of key stabilizing residues from the C-loop and F-loop of the wild-type α7/AChBP during the course of MD simulation. Fig. S2 shows the time evolution of interatomic distances between the associating calcium ion and the oxygen atoms of key stabilizing residues from the C-loop and F-loop of the E158A mutant of α7/AChBP. Fig. S3 shows the time evolution of the interatomic distances between the associating calcium ion and the oxygen atoms of key stabilizing residues from the C-loop and F-loop of the E185Q mutant of α7/AChBP. Fig. S4 shows the time evolution of the interatomic distances between the associating calcium ion and the oxygen atoms of key stabilizing residues from the C-loop and F-loop of the D160S mutant of α7/AChBP.

Results

Single-channel recordings

To investigate calcium potentiation at the single-channel level, we recorded ACh-elicited single-channel currents from mammalian fibroblasts transfected with cDNAs encoding the human α7 nAChR plus the chaperone NACHO, an endoplasmic reticulum resident protein required for export of α7 to the plasma membrane in nonneuronal cells (Gu et al., 2016). To register the inherently brief channel openings by the α7 nAChR, we applied our previously described methods for improved resolution of single-channel dwell times (Mukhtasimova et al., 2016). Briefly, single-channel currents were recorded in the cell-attached patch configuration, which enhances patch stability and reduces background noise, with a membrane potential of −100 mV, a sampling interval of 0.2 µs, and a digital Gaussian filter of 25 kHz. In the absence of divalent cations plus 1 mM EGTA, a relatively low concentration of ACh (10 µM) elicits infrequent channel openings with durations spanning from ∼10 to ∼200 µs (Fig. 1 a). However, in the presence of 10 µM ACh and calcium, a recording from a second patch of membrane from the same cell reveals a marked increase in the incidence of channel openings and an increase in the durations of the longest openings, which approach 1 ms (Fig. 1 b). Similarly, in the presence of 10 µM ACh and barium, a calcium surrogate, a recording from a third patch of membrane from the same cell again reveals a marked increase in the incidence of channel openings and an increase in the durations of the longest openings, which approach 1 ms (Fig. 1 c). Measurements of the current amplitude for the population of channel openings from each patch reveals a mean amplitude of 18.6 pA in the absence of divalent cations plus EGTA and reduced amplitudes of 14.5 and 14.3 pA in the presence of calcium and barium, respectively (P = 0.0025). The kinetic signatures of the infrequent and brief channel openings without calcium and the robust and longer channel openings with either calcium or barium were consistent from patch to patch and from cell to cell. For these three recordings, dwell time histograms of channel open durations are well described by the sum of two exponential components, with mean durations of ∼10 and ∼100 µs. However, in the presence of either calcium or barium, the relative weight of the component with longest mean duration increases (time constants and relative weights are listed in the Fig. 1 legend). Thus, the divalent cations calcium and barium increase the frequency of channel opening and prolong the durations of the openings.

Single-channel currents recorded in the outside-out patch configuration

In Fig. 1, all three recordings were obtained from the same cell but, owing to use of the cell-attached patch configuration, each recording monitored activity from a different patch of membrane. To demonstrate calcium potentiation of receptors within the same patch of membrane, we recorded single-channel currents from cell-free outside-out patches (Hamill et al., 1981). In addition, we used rapid solution exchange techniques (Liu and Dilger, 1991; Corradi et al., 2009) to remove and reapply calcium in the continued presence of ACh and thus assess reversibility of calcium potentiation. A recording from an exemplar outside-out patch containing the wild-type α7 nAChR, perfused with 10 µM ACh plus calcium, reveals robust single-channel openings throughout the first 30-s application period (Fig. 2). However, upon exchange into a solution containing 10 µM ACh without divalent cations, channel opening abruptly pauses and remains quiescent until exchange into the original solution containing ACh and calcium. This abrupt switching of channel opening activity is mirrored in a plot of the duration of each opening event against its time of occurrence during the recording; the plot also confirms that without calcium, channel openings are brief, whereas with calcium, channel openings are prolonged. However, owing to the greater background noise inherent to outside-out compared with cell-attached patches, the frequency bandwidth is reduced for outside-out patches; thus, calcium-dependent changes in mean open duration are best assessed using the cell-attached patches, as in Fig. 1. Nevertheless, successive recordings from the same patch of membrane confirm that calcium dramatically increases channel opening of the wild-type α7 nAChR and also demonstrate that calcium potentiation is reversible.

Single-channel recordings at increased ACh concentrations

Owing to the low potency of ACh in activating α7, only a subset of its five identical ligand binding sites is expected to be occupied in regions distant from cholinergic nerve terminals, providing a physiological rationale for calcium potentiation in extra-synaptic regions. However, for receptors in synaptic regions where the ACh concentration is much higher, a rationale

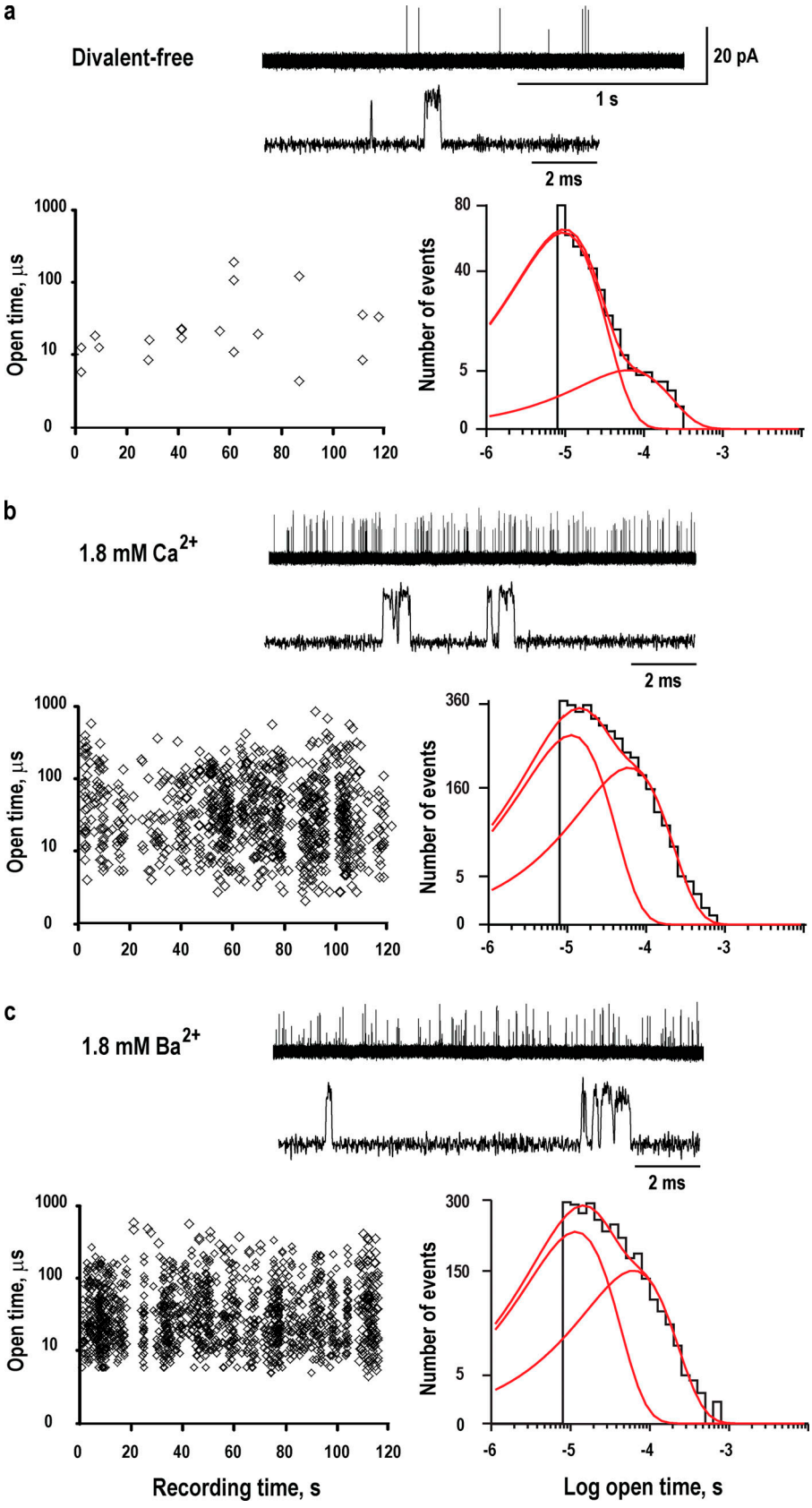

Figure 1. **Potentiation of the α7 nAChR by divalent ions at the single-channel level. (a)** Trace showing single-channel currents recorded in the presence of 10 µM ACh in the absence of divalent cations plus 1 mM EGTA. Recording was obtained in the cell-attached patch configuration with an applied potential of −100 mV and Gaussian filter of 25 kHz (see Materials and methods). Channel openings are upward deflections from baseline. Left: Plot of the durations of individual channel openings as a function of their time of occurrence during the recording. Right: A histogram of open dwell times fitted by the sum of two exponentials with the following time constants and relative weights: $\tau_0 = 1.2 \times 10^{-5}$ s, $a_0 = 0.855$; $\tau_1 = 9.9 \times 10^{-5}$ s, $a_1 = 0.145$. For the population of channel openings from this patch, the mean current amplitude was 18.6 ± 1.3 pA. **(b)** Trace showing single-channel currents in the presence of 10 µM ACh and 1.8 mM Ca^{2+}; the cell-attached patch for this recording was obtained from the same cell as in a. Left: Plot of the durations of individual channel openings as a function of time of occurrence during the recording. Right: A histogram of open dwell times fitted by the sum of two exponentials with the following time constants and relative weights: $\tau_0 = 1.4 \times 10^{-5}$ s, $a_0 = 0.658$; $\tau_1 = 8.3 \times 10^{-5}$ s, $a_1 = 0.342$. For the population of channel openings from this patch, the mean current amplitude was 14.5 ± 1.8 pA. **(c)** Trace showing single-channel currents in the presence of 10 µM ACh and 1.8 mM Ba^{2+}; the cell-attached patch for this recording was obtained from the same cell as in a and b. Left: Plot of the durations of individual channel openings as a function of time of occurrence during the recording. Right: A histogram of open dwell times fitted by the sum of two exponentials with the following time constants and relative weights: $\tau_0 = 1.2 \times 10^{-5}$ s, $a_0 = 0.611$; $\tau_1 = 9.7 \times 10^{-5}$ s, $a_1 = 0.389$. For the population of channel openings from this patch, the mean current amplitude was 14.3 ± 2.0 pA.

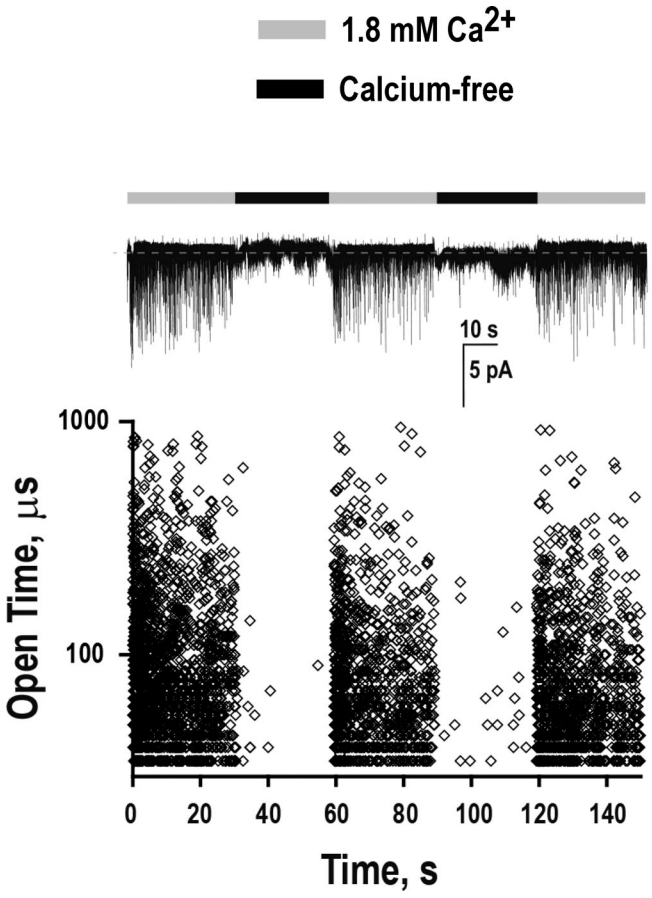

Figure 2. **Calcium potentiation demonstrated in the outside-out patch configuration.** Top: Continuous recording of current as a function of time from an outside-out patch containing wild-type α7 nAChRs at a holding potential of −70 mV and bandwidth of 7 kHz. Gray bars indicate perfusion with a solution containing 10 µM ACh and 1.8 mM Ca^{2+}, whereas black bars indicate perfusion with 10 µM ACh without calcium. Bottom: The durations of individual channel openings are plotted as a function of time of occurrence during the recording.

for calcium potentiation is less clear. Thus, we compared calcium potentiation of single-channel currents from limiting low to high ACh concentrations; the recordings were made in the cell-attached patch configuration to enable the utmost in patch stability and temporal resolution of the brief channel openings. In the absence of calcium, a limiting low concentration of 1 µM ACh elicits only rare channel openings, which appear at a frequency of approximately one every 30 s in a typical patch (Fig. 3 a, upper left). However, in the presence of 1 µM ACh plus calcium, the frequency of channel openings is increased (Fig. 3 a, lower left); expressed as the average from four to six independent patches for each condition (Fig. 3 a, left-middle), this increase in frequency is significant ($P < 0.03$), suggesting any patch-to-patch variation in opening frequency is smaller than the increase in opening frequency mediated by calcium. Dwell time histograms show a calcium-dependent increase in open durations, which are fitted by a single brief exponential component in the absence of calcium and two components in its presence (Fig. 3 a, right-middle; and Table 1); for the overall population of channel openings, the average open duration increases by approximately fourfold in the presence of calcium (Fig. 3 a, right).

Increasing the ACh concentration to 10 µM markedly increases the incidence of channel openings, both in the absence and presence of calcium (Fig. 3 b, left). However, the incidence in the presence of calcium is much greater than in its absence (Fig. 3 b, left-middle), as also shown in Figs. 1 and 2. Histograms of open durations exhibit two exponential components either without or with calcium but, with calcium, the relative weight of the component with longest mean duration increases (Fig. 3 b, right-middle; and Table 1), resulting in an increase in the average duration of channel openings (Fig. 3 b, right). In addition, periods of robust channel opening are occasionally interspersed by periods of reduced opening frequency (Fig. 3 b, lower left). Such quiescent periods were most apparent in the presence of calcium, and although a given patch contains multiple receptors, the quiescent periods suggest enhanced entry into a long-lived desensitized state.

In contrast to recordings obtained in the presence of 1 and 10 µM ACh, in the presence of 100 µM ACh, the incidence of channel openings is robust either without or with calcium (Fig. 3 c), and the average frequency of channel opening is not different without or with calcium ($P < 0.3$; Fig. 3 c, left-middle). Histograms of channel open dwell times exhibit two exponential components, with mean durations and relative weights that are similar without or with calcium (Fig. 3 c, right-middle, and Table 1), and the average duration of channel openings is not different without or with calcium ($P < 0.45$; Fig. 3 c, right). As observed in the presence of 10 µM ACh (Fig. 3 b), in the presence of calcium, periods of robust channel opening are occasionally interspersed by periods of reduced opening frequency, again suggesting enhanced entry into a desensitized state.

In summary, at low and intermediate ACh concentrations, where the fractional occupancy of the five ligand binding sites is expected to be low, both the frequency of channel openings and the average duration of the openings are increased by calcium. However, at a high ACh concentration, where the fractional occupancy of the ligand binding sites is expected to increase, the potentiating effect of calcium is not apparent at the single-channel level.

MD simulations

To identify structural counterparts of calcium potentiation of the α7 nAChR, we performed MD simulations using the crystal structure of an α7 ligand binding domain chimera composed of α7 and AChBP sequences in the presence of calcium ions. The α7/AChBP chimera shares 64% sequence identity with the ligand binding domain of human α7, and in the assembled pentamer, the majority of solvent accessible residues is derived from α7 (Li et al., 2011). Prior to simulation, a system ensemble was generated comprising one copy of the α7/AChBP pentamer, TIP3P water molecules, sodium, and chloride ions at an effective concentration of 150 mM, and randomly placed calcium ions and charge-neutralizing anions. The system ensemble was subjected successively to 10,000 steps of energy minimization, 5 ns of equilibration, and an MD production simulation of 150 ns under conditions of constant number, pressure, and temperature (see

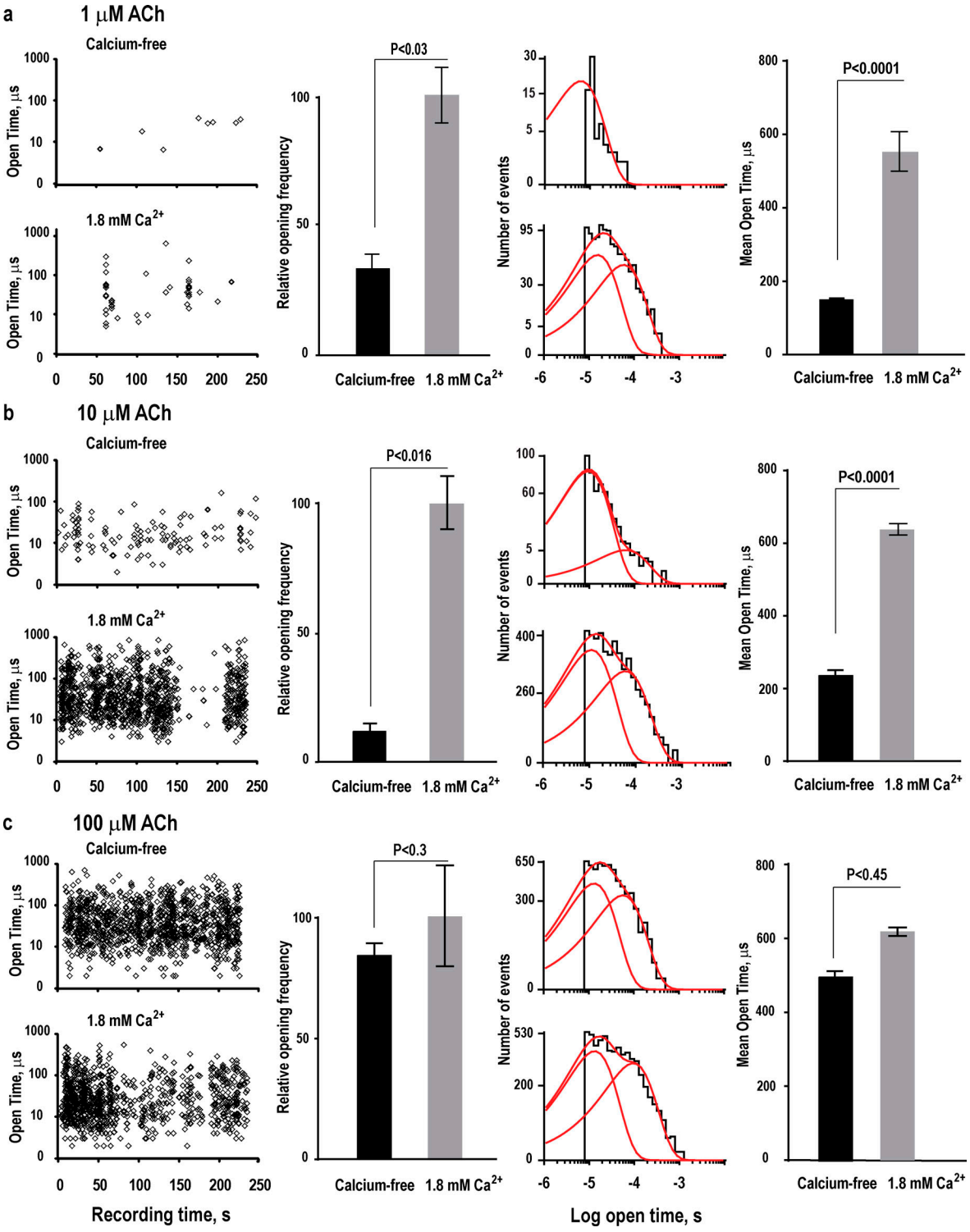

Figure 3. **Calcium potentiation depends on the ACh concentration. (a)** Left: Plot of the durations of individual channel openings in the presence of 1 μM ACh as a function of time of occurrence during the recording, without or with 1.8 mM Ca^{2+}. Recordings were obtained in the cell-attached patch configuration with an applied potential of −100 mV and Gaussian filter of 25 kHz. Left-middle: Comparison of the average channel opening frequency without or with 1.8 mM Ca^{2+}, obtained from four to six patches for each condition; channel opening frequency is expressed relative to that in the presence of 1.8 mM Ca^{2+}. Right-middle: Comparison of histograms of open dwell times fitted by the sum of either one or two exponentials, without or with 1.8 mM Ca^{2+}, respectively. Right: Comparison of the average duration of channel openings without divalent cations or with 1.8 mM Ca^{2+}. **(b and c)** Results are shown as in a, but with ACh concentrations of 10 (b) and 100 (c) μM. Error bars represent the SEM.

Table 1. **Distributions of open durations for wild-type α7 nAChR**

[ACh]	Calcium free				1.8 mM Ca^{2+}			
	Mean open, s		Weight		Mean open, s		Weight	
1 μM	$1.2 \times 10^{-5} \pm 1.7 \times 10^{-6}$		1.0		$1.5 \times 10^{-5} \pm 3.7 \times 10^{-6}$	$1.0 \times 10^{-4} \pm 9.7 \times 10^{-6}$	0.67 ± 0.02	0.33 ± 0.02
	n = 3				*n* = 6			
10 μM	$1.0 \times 10^{-5} \pm 1.2 \times 10^{-6}$	$6.1 \times 10^{-5} \pm 6.4 \times 10^{-6}$	0.90 ± 0.03	0.10 ± 0.06	$1.1 \times 10^{-5} \pm 1.3 \times 10^{-6}$	$1.2 \times 10^{-4} \pm 3.4 \times 10^{-5}$	0.58 ± 0.06	0.41 ± 0.06
	n = 6				*n* = 4			*n* = 4
100 μM	$1.2 \times 10^{-5} \pm 1.6 \times 10^{-6}$	$8.9 \times 10^{-5} \pm 1.6 \times 10^{-6}$	0.55 ± 0.03	0.45 ± 0.3	$1.2 \times 10^{-5} \pm 1.7 \times 10^{-6}$	$9.5 \times 10^{-5} \pm 8.5 \times 10^{-6}$	0.59 ± 0.04	0.41 ± 0.04
	n = 6				*n* = 6			

Time constants and relative weights of exponential components were obtained by fitting open-duration histograms for *n* experiments.

Materials and methods). The time course of the all-atom RMSD of the simulated relative to the initial structure shows an increase followed by a stable plateau that extends to the conclusion of the simulation (Fig. 4 a). The average structure between 80 and 100 ns of the simulation reveals five calcium ions bound to the α7/AChBP pentamer (Fig. 4 b), with each cation lodged at an interface between subunits and coordinated by anionic and polar side chains at the periphery of the ligand binding sites (Fig. 4 c). The residues coordinating calcium include Glu185 from the C-loop at the principal face of the ligand binding site and Glu158, Asp160, and Ser162 from the F-loop at the complementary face of the site. Time courses of the interatomic distance between an associating calcium ion and its target residues reveal a period of ∼60 ns during which the interatomic distances are large and fluctuate widely, followed by a period with reduced and stable interatomic distances extending to 150 ns (Fig. 4 d); time courses of association for the other four calcium ions are qualitatively similar to those in Fig. 4 d (Fig. S1). Thus, MD simulation reveals the association of five calcium ions, each coordinated by anionic and polar residues from the principal and complementary faces of each ligand binding site; these residues emerge as candidates for mediating calcium potentiation of the α7 nAChR.

To gain insight into contributions of electrostatic forces to the association between calcium and the anionic and polar residues at each subunit interface, we generated a 100-ns MD simulation of the α7/AChBP pentamer in the absence of calcium, solved the Poisson-Boltzmann equation for the final simulated structure, and mapped the electrostatic potential on the surface of the structure (see Materials and methods). The map reveals a region of strongly negative electrostatic potential at subunit interfaces that encompasses the key residues that coordinate calcium (Fig. 5, boxed region). We then introduced in silico mutations of each key anionic residue, generated a 100-ns MD simulation for each mutant, and mapped the electrostatic potential on the surface of the final structures. For the mutations D160S and E185Q, the electrostatic potential within the boxed region diminishes markedly compared with that for the wild-type α7/AChBP pentamer (Fig. 5), despite neutralizing only one of three local anionic residues in each case. By contrast, for the mutation E158A, the electrostatic potential within the boxed region remains strongly negative. These results predict that MD simulations of the mutant α7/AChBP pentamers in the presence of calcium will show diminished or no association for the D160S and E185Q mutants, but strong association for the E158A mutant.

MD simulations of mutant α7/AChBP pentamers in the presence of calcium

To evaluate expectations based on electrostatic surface potential, we performed MD simulations of the mutant α7/AChBP pentamers in the presence of calcium ions. For the E158A mutant, following energy minimization, equilibration, and an MD production simulation of 150 ns, the RMSD relative to the initial structure reaches a stable plateau, and each of the five subunit interfaces contains a calcium ion coordinated by the same anionic and polar residues identified in the simulation of the wild-type α7/AChBP: Glu185, Asp160, and Ser162 (Fig. 6, a–c). Time courses of the interatomic distances between an associating calcium ion and its target residues reveal a period of ∼80 ns of large and fluctuating interatomic distances, followed by a period with markedly reduced and stable interatomic distances extending to 150 ns (Fig. 6 d); similar time courses of association are observed for the other four calcium ions (Fig. S2). Thus, in accord with maintenance of a localized and strong electrostatic surface potential for the E158A mutant, MD simulation reveals a calcium ion coordinated by the same key anionic or polar residues from the principal and complementary faces of each ligand binding site, suggesting Glu158 does not contribute to calcium association linked to potentiation of the α7 nAChR.

By contrast to wild-type α7/AChBP and the E158A mutant, MD simulations of the E185Q and D160S mutants in the presence of calcium ions show large and fluctuating interatomic distances between the calcium ions and key anionic and polar residues throughout 100 ns of simulation (Fig. 6, e and f); similar time courses are observed for the other four calcium ions (Fig. S3 and Fig. S4). Thus, as suggested by analyses of electrostatic surface potential, either the E185Q or the D160S mutation is sufficient to prevent stable association of calcium with α7/AChBP, despite neutralizing only one of three local anionic residues in each case,

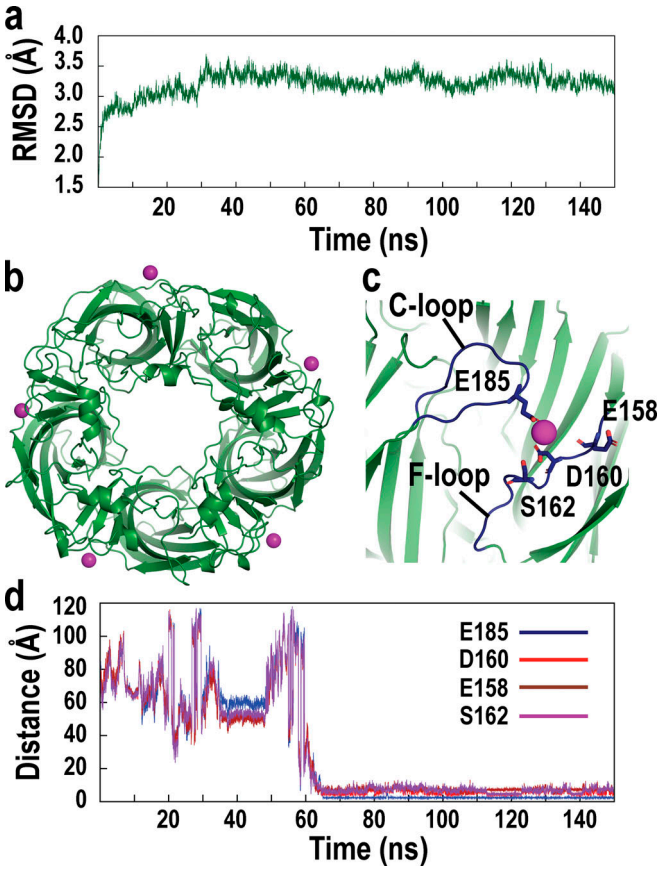

Figure 4. **Identification of candidate Ca^{2+} binding sites by MD simulation. (a)** Time evolution of the all-atom RMSD of the α7/AChBP pentamer in the presence of Ca^{2+} ions. **(b)** Structure of the α7/AChBP pentamer with bound Ca^{2+} ions at the conclusion of a 150-ns MD simulation. View is from the top of the pentamer, with Ca^{2+} ions shown as purple spheres at each subunit interface. **(c)** Ca^{2+} ion bound to one subunit interface is shown with key stabilizing residues depicted in stick representation; view is from the side of the pentamer. **(d)** Time evolution of the interatomic distances between the Ca^{2+} ion that ultimately associates and the oxygen atoms of key stabilizing residues from the C-loop and F-loop during the course of MD simulation.

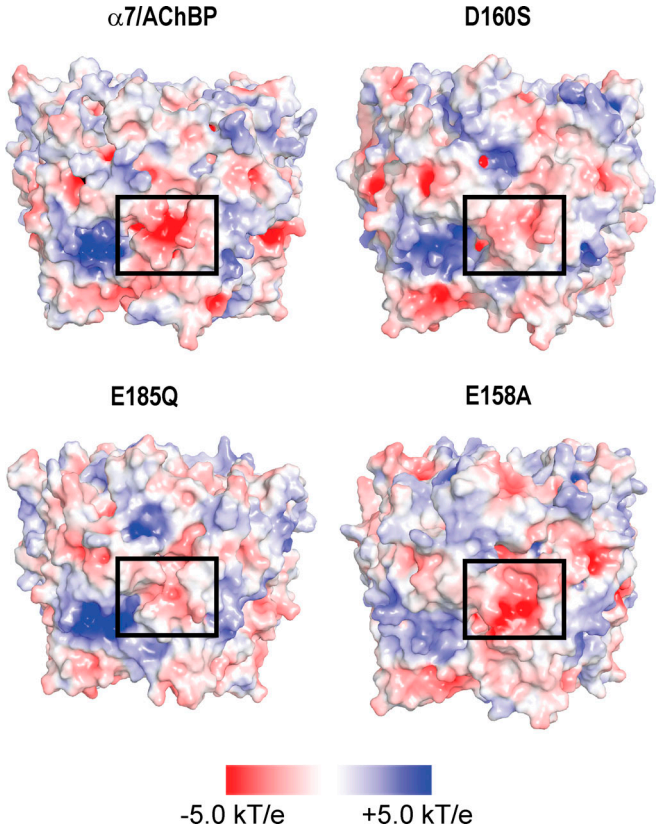

Figure 5. **Electrostatic analysis of wild-type and mutant α7/AChBP pentamers in the absence of calcium.** Each structure shows the electrostatic surface potential, computed by solving the Poisson-Boltzman equation, for the structure obtained following a 100-ns MD simulation. Boxed regions encompass residues observed to coordinate Ca^{2+} in Fig. 4. Red patches represent negative electrostatic potential, blue patches represent positive potential, and white patches represent neutral potential. The mutations D160S and E185Q reduce the negative electrostatic surface potential around the calcium binding site, whereas the E158A mutation maintains a negative electrostatic surface potential at the site. kT/e, electrostatic potential.

suggesting both Glu185 and Asp160 contribute to calcium binding linked to potentiation of α7.

Single-channel recordings from mutant α7 nAChRs

To test predictions from the MD simulations, we generated mutations of each anionic residue in the full-length human α7 nAChR and recorded single-channel currents from cell-attached patches, either without or with calcium. For the mutation E158A in the presence of 10 µM ACh without calcium, channel opening is infrequent, whereas in the presence of 10 µM ACh with calcium, channel opening is robust (Fig. 7 a, left), similar to the profile observed for the wild-type α7 nAChR. The channel opening frequency, assessed from four to six patches for each condition, increases in the presence of calcium ($P < 0.018$; Fig. 7 a, left-middle). Histograms of open dwell times are fitted by the sum of two exponential components without and three components with calcium (Fig. 7 a, right-middle; and Table 2), and the average duration of channel openings is prolonged in the presence of calcium ($P < 0.0001$; Fig. 7 a, right). Together, the results from MD simulation and single-channel recording show that calcium binds to and potentiates the α7 nAChR harboring the mutation E158A.

For the mutations E185Q and D160S in the presence of 10 µM ACh, channel opening is similar without or with calcium (Fig. 7, b and c, left columns). The channel opening frequency, assessed from four to six patches for each condition, is not different without or with calcium ($P < 0.37$, Fig. 7 b; $P < 0.11$, Fig. 7 c). Histograms of open dwell times are fitted by the sum of three exponentials for the E185Q mutant and two exponentials for the D160S mutant; for both mutants, the histograms are very similar without or with calcium (Fig. 7, b and c, middle-right columns; and Table 2), and the average duration of channel openings is not different without or with calcium ($P < 0.44$, Fig. 7 b; $P < 0.46$, Fig. 7 c). Thus, for the E185Q and D160S mutants, calcium does not increase the frequency of channel opening, nor does it prolong the average duration of channel openings. Together, MD simulations and single-channel recordings show that both Glu185 and Asp160 are required for calcium association linked to potentiation of the α7 nAChR.

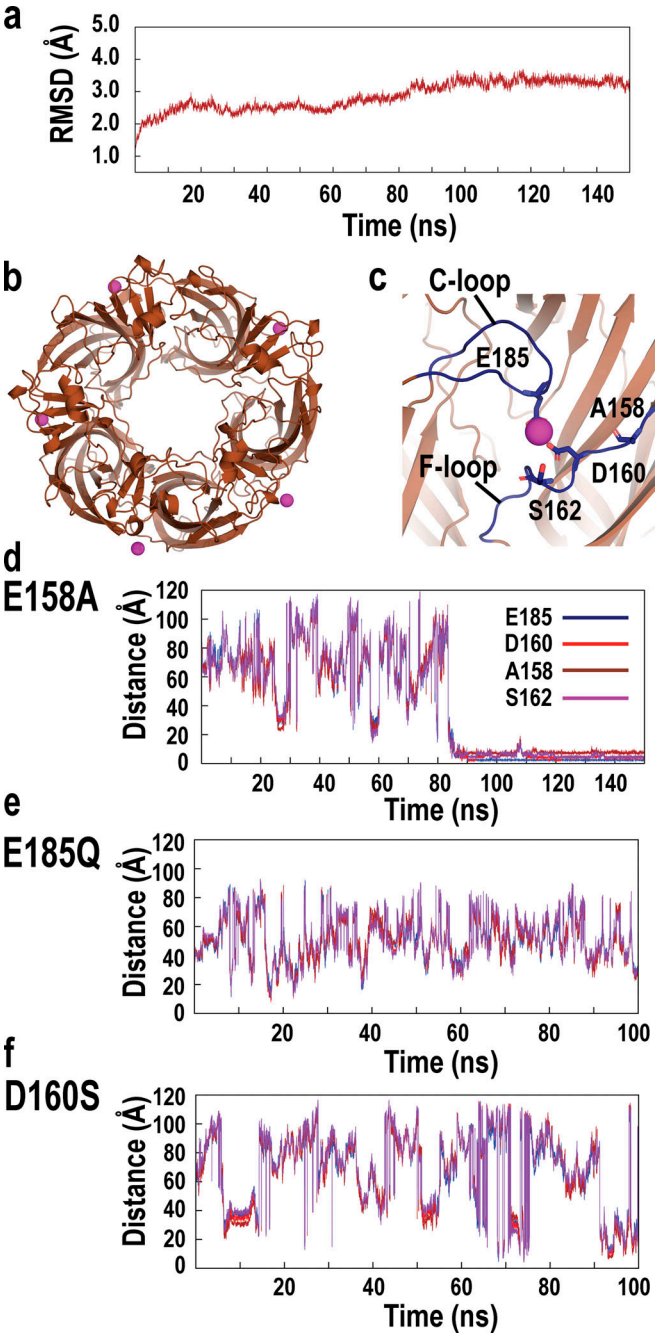

Figure 6. **MD simulations of in silico mutations of α7/AChBP in the presence of Ca^{2+} ions. (a)** Time evolution of the all-atom RMSD of the E158A mutant of the α7/AChBP pentamer in the presence of Ca^{2+} ions. **(b)** Structure of the E158A mutant of α7/AChBP with bound Ca^{2+} ions at the conclusion of a 150-ns MD simulation. View is from the top of the pentamer, with Ca^{2+} ions shown as purple spheres at each subunit interface. **(c)** Ca^{2+} ion bound to one subunit interface of the E158A mutant is shown with key stabilizing residues depicted in stick representation; view is from the side of the pentamer. **(d)** Time evolution of the interatomic distances between the associating Ca^{2+} ion and the oxygen atoms of key stabilizing residues from the C-loop and F-loop during the course of MD simulation. **(e and f)** Time evolution of the interatomic distances between the Ca^{2+} ion and the oxygen atoms of key stabilizing residues from the C-loop and F-loop from the E185Q and D160S mutants during the course of MD simulation.

Macroscopic currents recorded from wild-type and mutant α7 nAChRs

To corroborate results from single-channel recordings from the wild-type and mutant α7 nAChRs, we recorded whole-cell macroscopic currents elicited by either 10 or 100 µM ACh, without or with calcium. For each experiment, ACh was applied successively to the same cell with calcium, without calcium, and again with calcium, with 10-s recovery periods between each application (see Materials and methods). A different cell from the same transfection was used for each ACh concentration. For the wild-type α7 nAChR, application of 10 µM ACh with calcium elicits a robust macroscopic current that rises slowly and remains steady throughout the application period (Fig. 8 a). However, a second application of ACh without calcium elicits a markedly reduced current. A third application of ACh with calcium elicits a robust current with an amplitude equal to that in the first application, confirming that calcium potentiation is reversible, as also shown in Fig. 2. Comparison of the peak macroscopic currents for several independent cells confirms the strong potentiating action of calcium in the presence of 10 µM ACh (Fig. 8 a, right). By contrast, when the ACh concentration is increased to 100 µM, the current rises rapidly and decays bi-exponentially, either without or with calcium, and the amplitude of the current at its peak is indistinguishable without or with calcium. The decay of the current from its peak is due to desensitization, but the time course of the decay is not considered an accurate measure of desensitization onset kinetics owing to nonuniform agonist application inherent to the whole-cell recording mode, combined with the fast desensitization kinetics of α7. These results from whole-cell recording corroborate the results from single-channel recording, showing that calcium reversibly potentiates responses of the wild-type α7 nAChR activated by low but not high ACh concentrations (Fig. 3).

Our simulations show that the E158A mutant retains the ability to bind calcium, and single-channel recordings show that calcium potentiates currents elicited by 10 µM ACh. For the E158A mutant, whole-cell macroscopic currents elicited by 10 µM ACh show robust current with calcium, markedly reduced current without calcium, and fully recovered current upon reapplication of ACh with calcium (Fig. 8 b). By contrast, currents elicited by 100 µM ACh are indistinguishable with or without calcium. On the other hand, for the E185Q and D160S mutants, our simulations show that calcium does not associate with either mutant, and single-channel recordings show that calcium does not potentiate currents elicited by 10 µM ACh. For both the E185Q and D160S mutants, whole-cell macroscopic currents, elicited by either 10 or 100 µM ACh, are robust without or with calcium, and recordings from independent cells show no difference between the amplitudes of the currents without or with calcium ($P = 0.68$ and 0.26, Fig. 8 c; $P = 0.65$ and 0.22, Fig. 8 d). Thus, recordings of macroscopic currents corroborate the results from MD simulations and single-channel recordings, showing that E185 and D160, but not E158, are required for calcium association linked to potentiation of the α7 nAChR.

Structural changes upon calcium association

To gain insight into calcium-mediated structural changes in the α7 nAChR, we superimposed averaged structures of α7/AChBP,

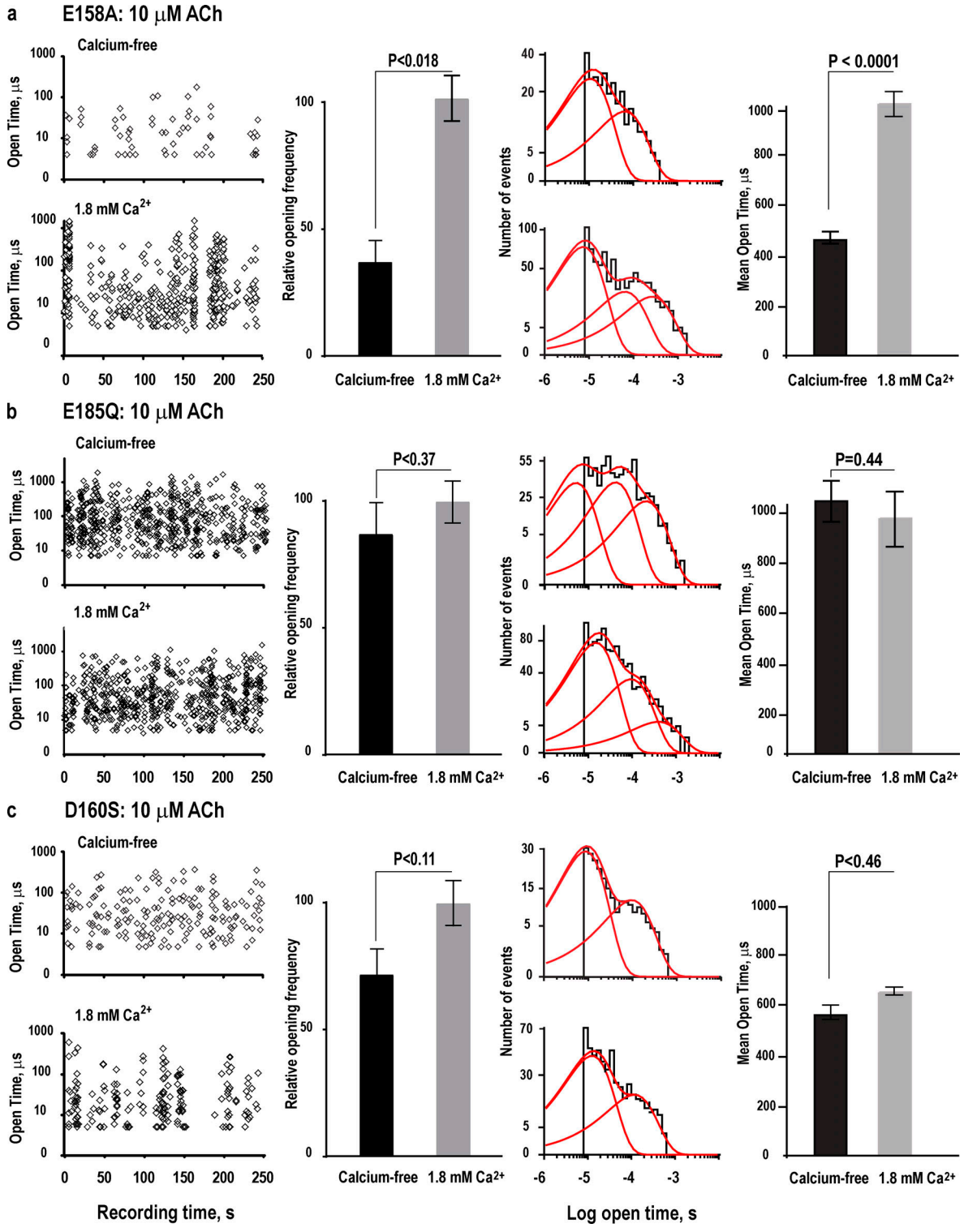

Figure 7. **Functional consequences of mutating candidate residues for Ca^{2+} association in the α7 nAChR. (a)** Left: For the mutation E158A, plot of the durations of individual channel openings in the presence of 10 μM ACh as a function of time of occurrence during the recording without or with 1.8 mM Ca^{2+}. Recordings were obtained in the cell-attached patch configuration with an applied potential of −100 mV and Gaussian filter of 25 kHz. Left-middle: Comparison of the average channel opening frequency without or with 1.8 mM Ca^{2+}, obtained from four to six patches for each condition; channel opening frequency is expressed relative to that in the presence of 1.8 mM Ca^{2+}. Right-middle: Comparison of histograms of open dwell times fitted by the sum of two or three exponentials without or with 1.8 mM Ca^{2+}, respectively. Right: Comparison of the average duration of channel openings without or with 1.8 mM Ca^{2+}. **(b and c)** Results are shown as in a, but for the mutations E185Q and D160S, respectively. Error bars represent the SEM.

Table 2. **Distributions of open durations for mutant α7 nAChRs**

	Calcium free						1.8 mM Ca^{2+}					
	Mean open, s			Weight			Mean open, s			Weight		
α7 E158A	$1.0 \times 10^{-5} \pm 1.1 \times 10^{-6}$	$8.2 \times 10^{-5} \pm 7.3 \times 10^{-6}$		0.74 ± 0.02	0.26 ± 0.02		$9.9 \times 10^{-6} \pm 1.1 \times 10^{-6}$	$2 \times 10^{-5} \pm 7.3 \times 10^{-6}$	$3.3 \times 10^{-4} \pm 4.5 \times 10^{-6}$	0.54 ± 0.05	0.33 ± 0.06	0.12 ± 0.03
	$n = 4$						$n = 4$					
α7 E185Q	$6.8 \times 10^{-6} \pm 2.3 \times 10^{-5}$	$5.0 \times 10^{-5} \pm 2.3 \times 10^{-6}$	$2.4 \times 10^{-4} \pm 5.3 \times 10^{-5}$	0.40 ± 0.02	0.37 ± 0.02	0.23 ± 0.03	$9.4 \times 10^{-6} \pm 2.0 \times 10^{-5}$	$6.5 \times 10^{-5} \pm 2.7 \times 10^{-6}$	$2.8 \times 10^{-4} \pm 3.8 \times 10^{-6}$	0.50 ± 0.09	0.39 ± 0.05	0.10 ± 0.06
	$n = 4$						$n = 4$					
α7 D160S	$1.0 \times 10^{-5} \pm 1.0 \times 10^{-6}$	$1.1 \times 10^{-4} \pm 1.0 \times 10^{-5}$		0.69 ± 0.03	0.30 ± 0.03		$1.0 \times 10^{-5} \pm 1.6 \times 10^{-6}$	$3.3 \times 10^{-4} \pm 1.7 \times 10^{-5}$		0.71 ± 0.03	0.28 ± 0.03	
	$n = 4$						$n = 4$					

Time constants and relative weights of exponential components were obtained by fitting open duration histograms for *n* experiments. Duration values are mean open ± SD.

as well as those of the E158A mutant, either without or with calcium ions, from the final 20 ns of the MD simulations. Comparing the calcium-bound relative to the calcium-free structures reveals that the C-loop and F-loop are drawn together toward the bound calcium ion; similar structural changes are observed for both the wild-type α7/AChBP and the E158A mutant (Fig. 9, a and b). These calcium-induced changes in the C-loop and F-loop are analogous to those observed by comparing Apo and epibatidine-bound structures of α7/AChBP (40) but are smaller in magnitude.

The local structural changes at the site of calcium association could propagate throughout the pentamer, resulting in a global structural change that contributes to calcium potentiation. To assess whether calcium promotes a change in the global structure of the ligand binding domain, we computed the R_g as a function of simulation time (Fig. 9 c); the R_g is a measure of the distribution of atoms and their masses relative to the center of mass of a protein and provides a measure of global structural compactness (see Materials and methods). For the simulation of wild-type α7/AChBP without calcium, the time course of the R_g shows an initial increase followed by a stable plateau. In the simulation with calcium, the time course of the R_g shows an initial increase but then a decrease as successive calcium ions bind (Fig. S1), and by the conclusion of the simulation, the R_g is reduced compared with that in the calcium-free simulation. The divergence of the two structures indicates that calcium binding promotes an increase in protein compactness; a simulation time of 100 ns likely underestimates the divergence between the two structures compared with that ultimately achieved at steady state.

For the simulation of the E158A mutant, the time course of the R_g without calcium shows an initial increase, whereas the simulation with calcium shows an initial decrease, as observed for wild-type α7/AChBP (Fig. 9 d). However, following the initial divergence, the profiles for the two simulations merge despite the continued association of calcium ions in the corresponding simulation (Fig. S2). We speculate that the similar R_g values at 100 ns arise from incomplete structural rearrangements of the F-loop owing to the substitution of the small and hydrophobic Ala for the larger and anionic Glu; given that calcium remains associated in the E158A mutant, a simulation of longer duration would likely be required to distinguish whether the R_g with calcium diverges from that without calcium at steady state.

For the simulations of the E185Q mutant, the time course of the R_g is largely indistinguishable with or without calcium, although with calcium the R_g shows an initial increase rather than a decrease, in contrast to wild-type α7/AChBP or the E158A mutant (Fig. 9 e). Ultimately, however, the R_g without and with calcium merge during the second half of the simulation for the E185Q mutant, in agreement with the absence of stable calcium association. For the simulations of the D160S mutant, the time course of the R_g is indistinguishable without or with calcium (Fig. 9 f), as anticipated from the absence of stable calcium association. Thus, MD simulations reveal local structural changes in the C-loop and F-loop upon coordination of calcium, and analyses of the R_g show that these local changes are associated with a global increase in compactness of the ligand binding domain. Although the increase in compactness is confined to the ligand binding domain and is likely incomplete, in the full-length α7 nAChR, changes in compactness in the ligand binding domain may give rise to structural changes in the pore domain.

Discussion

We show that extracellular calcium is a powerful potentiator of the human α7 nAChR activated by low but not high concentrations of ACh. Potentiation manifests as an increase in the frequency of channel openings together with an increase in the average duration of the openings. The dual effects of calcium on channel opening frequency and open durations predict more than an order of magnitude greater response to ACh in the presence compared with the absence of calcium, thus increasing cellular excitability and increasing intracellular calcium. MD simulations using the high-resolution structure of a surrogate of the α7 ligand binding domain show that calcium associates with a pair of anionic residues that frame the periphery of the ligand binding sites. Mutagenesis of the residues identified by

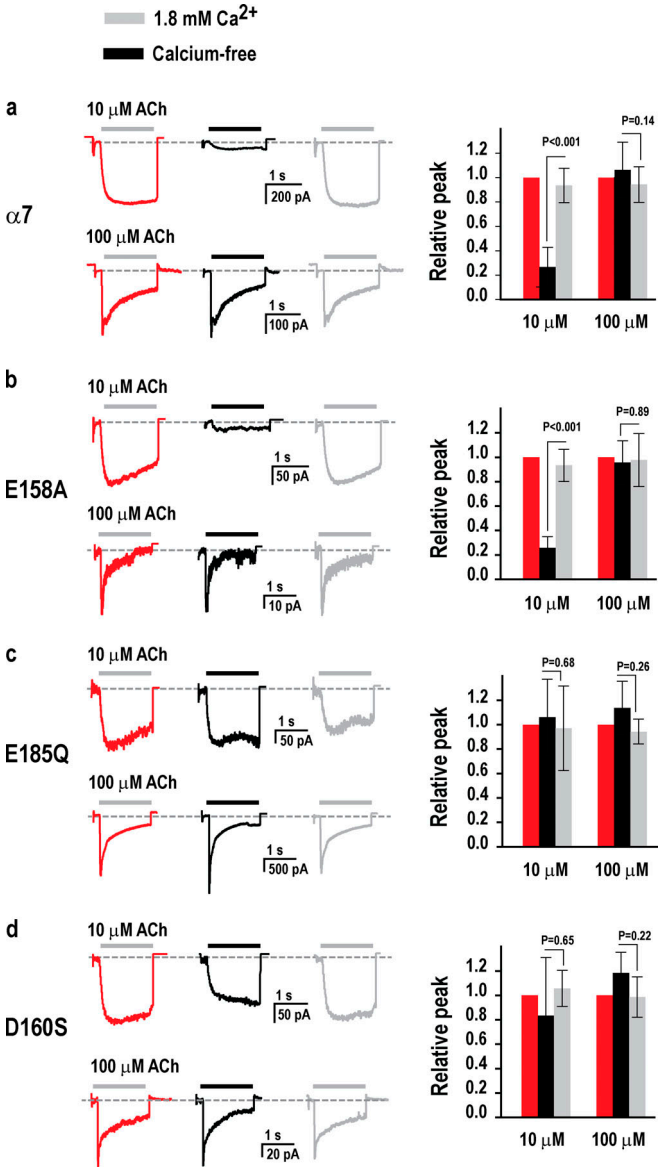

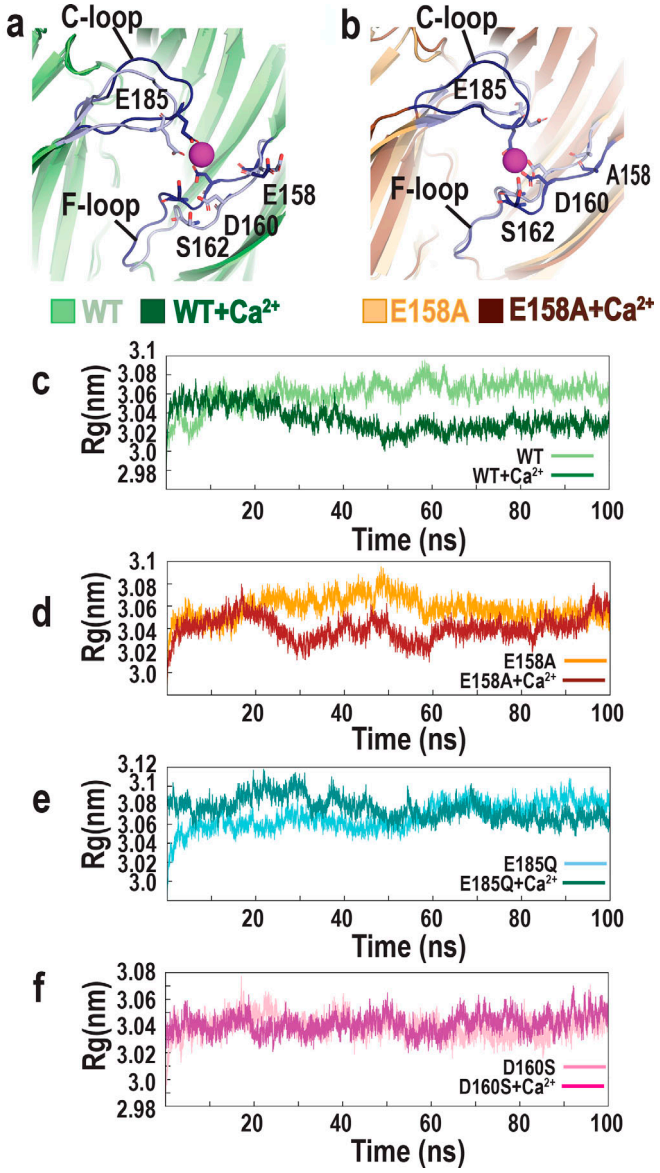

Figure 8. **Calcium potentiation of ACh-elicited macroscopic currents for wild-type and mutant α7 nAChRs. (a)** Left: Recordings of current as a function of time in the whole-cell configuration following successive 1.5-s applications of the indicated concentrations of ACh with, without, or with 1.8 mM Ca^{2+}, at a membrane potential of −50 mV and bandwidth of 5 kHz (see Materials and methods). Currents elicited by 10 and 100 µM ACh were recorded from different cells. For each cell, currents elicited by the same concentration of ACh were compared in the absence and presence of calcium. Right: Plots of the amplitude of the peak current averaged for four to six cells per condition. **(b–d)** Results are shown for the indicated mutants as in a. For wild-type α7 activated by 100 µM ACh, the time course of current decay is fitted by the sum of two exponential components: τ_{fast} = 70 ± 27 ms (relative area 0.47 ± 0.22) and τ_{slow} = 652 ± 296 ms (relative area 0.34 ± 0.20); *n* = 27. Error bars represent the SD.

Figure 9. **Local and global structural changes in wild-type and mutant α7/AChBP in the presence and absence of calcium. (a)** Superposition of averaged wild-type α7/AChBP structures following MD simulation in the presence (dark blue backbone) or absence (light blue backbone) of Ca^{2+}. Key residues are depicted in stick representation and the Ca^{2+} ion as a purple sphere. **(b)** Superposition of averaged E158A mutant α7/AChBP structures following MD simulation in the presence (dark blue backbone) or absence (light blue backbone) of Ca^{2+}. **(c–f)** Time evolution of the R_g for the indicated wild-type and mutant α7/AChBP structures in the presence or absence of Ca^{2+}.

simulation shows that each anionic residue is required for the potentiating action of calcium. The results suggest a novel role of calcium in extending the signaling range of ACh to extrasynaptic regions harboring α7 and in modulating signaling in those regions. Owing to the role of α7 in inflammatory, neurological, and neurodegenerative disorders, the molecular-level findings will be important toward therapeutic drug design. The results also raise further questions, including the stoichiometry of ACh and calcium occupancy associated with potentiation of α7, the precise anatomical location of α7 relative to calcium channels or transporters, and the consequences of α7-mediated calcium influx in activating intracellular second messengers.

Previous studies showed that calcium potentiates nAChRs from a variety of neuronal cells. In cells from the medial habenula

(Mulle et al., 1992), adrenal medulla (Vernino et al., 1992), and sympathetic ganglia (Amador and Dani, 1995), a physiological concentration of calcium increased the amplitude of macroscopic currents elicited by low to intermediate concentrations of agonist by two- to threefold. In neurons from the medial habenula, the increase in current was accompanied by a commensurate increase in single-channel opening frequency, without a change in open channel dwell times, as registered with a recording bandwidth of 2 kHz and dead time of 0.1 ms. However, in the present work with α7, the majority of channel openings would not have been resolved with a dead time of 0.1 ms (see Figs. 1, 3, and 7). In addition, in the recordings from the medial habenula, the channel open durations extended to tens of milliseconds, similar to those subsequently observed for the heteromeric α3β4 nAChR (Sine, et al., 2019), a major nAChR subtype in the medial habenula (Quick et al., 1999; Grady et al., 2009). Notably, recombinant α3β4 nAChRs expressed in *Xenopus laevis* oocytes showed calcium potentiation of macroscopic currents (Vernino et al., 1992). Thus, while calcium potentiation of nAChRs has been demonstrated in a variety of neurons, the types of nAChRs in these neurons were not established.

Calcium potentiation of the α7 nAChR was ultimately demonstrated in studies of recombinant α7 expressed in heterologous systems. Studies of α7 expressed in *Xenopus* oocytes showed that calcium increased the amplitude of macroscopic currents elicited by a relatively high concentration of ACh (100 µM; Eiselé et al., 1993), and studies of an α7/5-HT3 chimera showed that calcium increased the amplitude of currents elicited by saturating concentrations of ACh (Galzi et al., 1996). In the present work, we studied the full-length human α7 nAChR expressed in a human fibroblast cell line, implemented the utmost temporal resolution in single-channel recording, and complemented this with macroscopic current recordings coupled with rapid solution exchange techniques.

In contrast to expectations from previous studies of the α7 nAChR, we found that in the presence of low but not high concentrations of ACh, calcium increases the frequency of channel opening and increases the average duration of the openings. Furthermore, analyses of channel open dwell times reveal that in the absence of calcium, an exponential component with brief mean duration (~10 µs) predominates over a component with 10-fold longer mean duration, but that in the presence of calcium, the relative weight of the component with longer mean duration markedly increases. The increased channel opening frequency, combined with the increase in the average duration of channel openings, predicts that in regions distant from points of ACh release, calcium could potentiate responses to ACh by up to 20-fold. Thus, we conclude that under conditions in which the ACh concentration is low, calcium is a necessary cofactor in the activation of α7.

By leveraging the three-dimensional structure of a surrogate for the α7 ligand binding domain (Li et al., 2011) and subjecting it to MD simulation in the presence of calcium, we identify a novel mode of calcium association with α7. The simulations reveal that calcium bridges a pair of anionic residues, one from the principal face, Glu185 within the C-loop, and the other from the complementary face, Asp160 within the F-loop, that together

	Principal Face	Complementary Face
	E185	D160
α7 human	SERFYECCKEPYPD	QEADISGYIPNGEW
α7 chimp	SERFYECCKEPYPD	QEADISGYIPNGEW
α7 rat	NEKFYECCKEPYPD	QEADISSYIPNGEW
α7 bovine	SEKFYECCKEPYPD	QEADISGYIPNGEW
α7 cat	SEKFYECCKEPYPD	QEADISGYIPNGEW
α7 dog	SEKFYECCKEPYPD	QEADISGYIPNGEW
α7 elephant	SEKFYDCCKEPYPD	QEADISSYIPNGEW
α7 armadillo	SERFYDCCKEPYPD	QEADISGYIPNGEW
α7 opposum	SERFYDCCKEPYPD	QEADISGYISNGEW
α7 platypus	NERFYDCCKEPYPD	QEADVSGYISNGEW
α7 lizard	TETFYDCCKEPYPD	QEAEISGYISNGEW
α7 chick	TESFYECCKEPYPD	QEADISGYISNGEW
α7 finch	TESFYECCKEPYPD	QEADISGYISNGEW
α7 frog	SENYYECCKEPYLD	LESDISEYISNGEW
α7 zebrafish	NERFYDCCKEPYPD	IDADITGYIANGEW
α7 fugu	NEVFYDCCKEPYPD	NEADISGYMANGEW

	Principal Face	Complementary Face
	E185	D160
α1	HSVTYSCCPDTPYLD	DQPDLSNFMESGEW
α2	NSKKYDCCA-EIYPD	QTVDLKDYWESGEW
α3	HDIKYNCCE-EIYPD	SSMNLKDYWESGEW
α4	NTRKYECCA-EIYPD	SRVDQLDFWESGEW
α5	GNRTDSCC--W-YPY	QDVDKRDFFDNGEW
α6	HDIKYNCCE-EIYTD	SKVDMNDFWENSEW
α7	SERFYECCK-EPYPD	QEADISGYIPNGEW
α9	NVISYGCCS-EPYPD	DSGDLSDFIEDVEW
α10	RVLTYGCCS-EPYPD	AAASLADFVENVEW
β2	NENPD---D-STYVD	EVASLDDFTPSGEW
β3	GNRRDGVYS---YPF	ENVDRKDFFDNGEW
β4	TVNPQ---D-PSYVD	PTASMDDFTPSGEW

Figure 10. **Sequence alignments of residues within the principal and complementary faces of α7 subunits from different species (upper alignment) and from different types of human nAChR subunits (lower alignment).** Anionic residues conserved at positions equivalent to Glu185 and Asp160 are highlighted in red.

frame the entrance to the ligand binding site. Subjecting either residue to charge neutralization eliminates calcium potentiation, showing that this pair of anionic residues is required for calcium association linked to potentiation. An anionic residue, either Glu or Asp, is conserved at positions equivalent to Glu185 and Asp160 across α7 subunits from vertebrate species (Fig. 10), suggesting that the interaction of calcium with anionic residues from opposing subunits is a general structural feature of α7 potentiation.

Our study is the first to show that Glu185 within the C-loop is required for calcium stabilization linked to potentiation. By contrast to its sequence conservation in α7 across vertebrate species, Glu185 is not conserved across different types of human nAChR subunits; an anionic residue is present at equivalent positions of only the α4 and α2 subunits (Fig. 10). Potentially, these heteromeric α subunits could form a calcium binding site when paired with the β3 subunit, which contains an aspartate residue at the position equivalent to Asp160. However, predominant types of heteromeric nAChRs, such as α4β2 and α3β4, lack the pair of anionic residues at positions equivalent to Glu185 and Asp160. Thus, while the structural mode of calcium interaction depicted in Fig. 4 c and Fig. 9 a is required for potentiation

of α7, different structural modes of calcium interaction linked to potentiation remain to be discovered in other types of nAChRs.

Using an α7/5-HT3 chimera, Galzi et al. (1996) showed that a stretch of 12 residues within the F-loop of chick α7 was required for calcium potentiation, and that mutations of individual residues increased, decreased, or abolished potentiation. Notably, mutation of Glu172, corresponding to Glu169 in the α7/AChBP structure (Fig. 10), to glutamine eliminated calcium potentiation. However, high-resolution structures of nAChRs obtained subsequently show that Glu172 establishes an electrostatic interaction with the invariant residue Arg 209 (Walsh et al., 2018; Gharpure et al., 2019; Rahman et al., 2020), a key component of the principal coupling pathway linking agonist binding to channel gating (Lee and Sine, 2005; Mukhtasimova and Sine, 2013). While the local environment of Glu172 appears incompatible with forming a calcium binding site, Glu172 may instead contribute to coupling of calcium binding to potentiation. Mutation of the α7/5-HT3 residue Asp163, corresponding to Asp160 in α7/AChBP, to asparagine enhanced calcium potentiation, an effect contrary to ours and incompatible with simple electrostatic stabilization of calcium. Mutation of the α7/5-HT3 residue Ser169, corresponding to Pro166 in α7/AChBP, to glutamate enhanced calcium potentiation, which is compatible with electrostatic stabilization of calcium. However, the presence of Ser in chick and Pro in human α7 indicates that any contribution of Ser169 to potentiation would be species specific. Finally, mutation of the α7/5-HT3 residue Glu161, corresponding to Glu158 in α7/AChBP, to arginine did not affect calcium potentiation as we observed upon mutation of Glu158 to alanine. Major differences between the present work and that by Galzi et al. (1996) are that an α7/5-HT3 chimera was studied rather than the full-length human α7, and potentiation was assessed from changes in the magnitude of the macroscopic current elicited by a saturating concentration of ACh, rather than from changes in single-channel and macroscopic currents elicited by low and intermediate concentrations of ACh.

Our studies of the mutations E185Q and D160S suggest an additional, unexpected functional contribution of these residues. In particular, both mutants exhibited robust responses to ACh, and the average open durations were similar to those of the wild-type α7 nAChR in the presence of calcium (see Figs. 3 and 7). These observations seemed counterintuitive, because with calcium no longer able to potentiate, activation might be expected to approach that of wild-type α7 in the absence of calcium. However, while Glu185 and Asp160 are required for calcium potentiation, they may also contribute to the setpoint for activation. For wild-type α7 in the absence of calcium, electrostatic repulsion between the two residues may reduce the setpoint, reducing activation, whereas mutation of either residue would relieve the repulsion, thus increasing the setpoint and increasing activation.

Our observation that calcium potentiation depends on ACh concentration suggests a novel relationship between occupancy by ACh and calcium and the efficacy with which the α7 channel opens. At low concentrations of ACh, only a subset of the five identical ligand binding sites will be occupied so that calcium could bind to sites either with or without bound ACh. In this scenario, the major brief kinetic class of openings would be associated with receptors with low ACh occupancy, whereas the minor long kinetic class would be associated with receptors with increased ACh occupancy; the role of calcium, whether bound to sites with or without ACh, is to promote the long over the brief kinetic class of openings without affecting the stability of the open states. On the other hand, at high concentrations of ACh, the fractional occupancy by ACh will increase, which promotes the more stable kinetic class of channel openings; increased ACh occupancy thus supersedes any further stabilization provided by calcium binding. The stoichiometric and spatial relationships between occupancy by ACh and calcium and the kinetics of α7 channel gating thus emerge as essential questions for future study.

Although our results from mutagenesis combined with functional analyses corroborate the sites of calcium association identified by MD simulation, there could be additional calcium sites associated with potentiation. Our simulations were performed using the software NAMD that incorporates the CHARMM36m force field (see Materials and methods), which although state of the art, does not include polarizable interactions. While electrostatic interactions between inorganic cations and side chains with fixed electric charge are readily detected, interactions between inorganic cations and polarizable side chains are either underestimated or not detected. This issue is particularly relevant for calcium, a cation with high charge density for which modeling has been empirical (Zhang et al., 2020). Future simulations with improved modeling of the calcium ion and that include polarizable interactions (Inakollu et al., 2020) may allow more robust detection of potential calcium binding sites. In addition, the structure of α7/AChBP does not include the pore and cytoplasmic domains of the full-length α7 nAChR, and additional calcium binding sites could be elsewhere in the structure. For example, anionic residues within the lumen of the extracellular domain have been shown to contribute to calcium selectivity in ion permeation (Colón-Sáez and Yakel, 2014), although they have not been evaluated for contributions to potentiation. It is also possible that potentiation of α7 may depend jointly on calcium occupancy of the sites identified herein, as well as calcium sites not yet identified. Thus, while our study identifies sites of calcium association required for potentiation, additional sites of calcium association linked to potentiation are still possible.

Our MD simulations reveal not only sites of calcium binding, but also local and global conformational changes associated with calcium binding. The time length of our simulations is likely insufficient to reveal the full range of conformational changes in response to calcium binding, but the observed changes may provide a glimpse of the initial structural changes induced by calcium. The local conformational changes include displacement of the C-loop and F-loop toward the bound calcium ion, motions analogous to those induced by agonist (Celie et al., 2004; Hansen et al., 2005; Gao et al., 2005), while the global conformational changes show increased compactness of the ligand binding domain. The protein backbones stemming from both the C-loop and F-loop extend to the junction between the ligand binding and pore domains, providing a means to convey changes due to

calcium binding to the pore. In addition, the global conformational changes are reminiscent of the twisting motions revealed by superposition of crystal structures captured in apo and agonist bound states (Sauguet et al., 2014; Kaczanowska et al., 2014; Du et al., 2015; Basak et al., 2018; Masiulis et al., 2019); these global changes may be transmitted between the ligand binding and pore domains via the C-loop and F-loop, as well as the Cys-loop and β1-β2 loop, all of which span the junction between the binding and pore domains. Although the conformational changes due to calcium binding are likely smaller than those due to agonist binding (Li et al., 2011), these smaller changes may prime the receptor so that changes elicited by agonist are either more stable or occur more rapidly. A recent study in which MD simulations were applied to a model of the full-length α7 nAChR also revealed conformational changes in the presence of calcium that were consistent with a partially activated state (Suresh and Hung, 2019).

A classical paradigm in neurotransmitter signaling is point-to-point, rapid on and off synaptic transmission. A second, more recent paradigm is diffusion or volume transmission in which nerve-released neurotransmitter diffuses to spatially distant receptor targets (Descarries et al., 1997; Lendvai and Vizi, 2008). The slow on-and-off nature of volume transmission is well suited to slowly activating and inactivating metabotropic receptors, such as those for monoamine, indolamine, and peptide neurotransmitters. Volume transmission is also compatible with α7 signaling in extra-synaptic regions where calcium could potentiate activation by low ACh concentrations. Choline, a product of ACh hydrolysis, is an efficacious agonist for α7 (Alkondon et al., 1997), but its potency is lower than that of ACh, enabling only partial occupancy of the five binding sites on α7. Our results suggest that extracellular calcium compensates for low agonist occupancy, and that simultaneous occupancy by an organic and an inorganic cation increases both cellular excitation and calcium influx. The increased agonist efficacy conferred by calcium would promote activation of α7 nAChRs located distant from sites of ACh release, expanding the spatial range of signaling. In addition, extracellular calcium can be depleted transiently during periods of intense neuronal activity or pathological conditions, owing to the small volume of the neuropil in the context of calcium uptake processes (Egelman and Montague, 1999; Nicholson et al., 1977; Rusakov and Fine, 2003; Silver and Erecińska, 1990; Pumain et al., 1983). Finally, α7 may regulate its own activity through local and transient depletion of extracellular calcium owing to its high calcium permeability. Thus, the structure of α7 allows it to function as a coincidence detector for both ACh and calcium, enabling multifaceted modes of regulation.

Acknowledgments

Christopher J. Lingle served as editor.

We thank Daniel Jackson, Britson Paula, Garrison Timmer, and Haihua Liu of the Mayo Clinic Research Computing Facility for assistance in implementing hardware and software for MD simulations.

This research was supported by National Institutes of Health grant NS-094124 to S.M. Sine and grants from Universidad Nacional del Sur (PGI 24/B227) and Agencia Nacional de Promoción Científica y Tecnológica (PICT-2017 1720) to C. Bouzat.

The authors declare no competing financial interests.

Author contributions: K. Natarajan, N. Mukhtasimova, and M. Lasala recorded and analyzed single-channel currents; J. Corradi recorded and analyzed macroscopic currents; K. Natarajan conducted and analyzed MD simulations; S.M. Sine wrote the manuscript with contributions by C. Bouzat, K. Natarajan, and N. Mukhtasimova. S.M. Sine and C. Bouzat supervised research in their respective laboratories.

Submitted: 12 March 2020
Revised: 19 May 2020
Accepted: 22 June 2020

References

Alkondon, M., E.F.R. Pereira, W.S. Cortes, A. Maelicke, and E.X. Albuquerque. 1997. Choline is a selective agonist of α7 nicotinic acetylcholine receptors in the rat brain neurons. *Eur. J. Neurosci.* 9:2734–2742. https://doi.org/10.1111/j.1460-9568.1997.tb01702.x

Alkondon, M., E.F. Pereira, H.M. Eisenberg, and E.X. Albuquerque. 2000. Nicotinic receptor activation in human cerebral cortical interneurons: a mechanism for inhibition and disinhibition of neuronal networks. *J. Neurosci.* 20:66–75. https://doi.org/10.1523/JNEUROSCI.20-01-00066.2000

Amador, M., and J.A. Dani. 1995. Mechanism for modulation of nicotinic acetylcholine receptors that can influence synaptic transmission. *J. Neurosci.* 15:4525–4532. https://doi.org/10.1523/JNEUROSCI.15-06-04525.1995

Andersen, N., J. Corradi, S.M. Sine, and C. Bouzat. 2013. Stoichiometry for activation of neuronal α7 nicotinic receptors. *Proc. Natl. Acad. Sci. USA.* 110:20819–20824. https://doi.org/10.1073/pnas.1315775110

Baker, N.A., D. Sept, S. Joseph, M.J. Holst, and J.A. McCammon. 2001. Electrostatics of nanosystems: application to microtubules and the ribosome. *Proc. Natl. Acad. Sci. USA.* 98:10037–10041. https://doi.org/10.1073/pnas.181342398

Basak, S., Y. Gicheru, S. Rao, M.S.P. Sansom, and S. Chakrapani. 2018. Cryo-EM reveals two distinct serotonin-bound conformations of full-length 5-HT_{3A} receptor. *Nature.* 563:270–274. https://doi.org/10.1038/s41586-018-0660-7

Bosmann, H.B.. 1972. Acetylcholine receptor. I. Identification and biochemical characteristics of a cholinergic receptor of guinea pig cerebral cortex. *J. Biol. Chem.* 247:130–145.

Breese, C.R., C. Adams, J. Logel, C. Drebing, Y. Rollins, M. Barnhart, B. Sullivan, B.K. Demasters, R. Freedman, and S. Leonard. 1997. Comparison of the regional expression of nicotinic acetylcholine receptor alpha7 mRNA and [125I]-alpha-bungarotoxin binding in human postmortem brain. *J. Comp. Neurol.* 387:385–398. https://doi.org/10.1002/(SICI)1096-9861(19971027)387:3<385::AID-CNE5>3.0.CO;2-X

Broide, R.S., U.H. Winzer-Serhan, Y. Chen, and F.M. Leslie. 2019. Distribution of α7 Nicotinic Acetylcholine Receptor Subunit mRNA in the Developing Mouse. *Front. Neuroanat.* 13:76. https://doi.org/10.3389/fnana.2019.00076

Celie, P.H., S.E. van Rossum-Fikkert, W.J. van Dijk, K. Brejc, A.B. Smit, and T.K. Sixma. 2004. Nicotine and carbamylcholine binding to nicotinic acetylcholine receptors as studied in AChBP crystal structures. *Neuron.* 41:907–914. https://doi.org/10.1016/S0896-6273(04)00115-1

Colón-Sáez, J.O., and J.L. Yakel. 2014. A mutation in the extracellular domain of the α7 nAChR reduces calcium permeability. *Pflugers Arch.* 466:1571–1579. https://doi.org/10.1007/s00424-013-1385-y

Corradi, J., F. Gumilar, and C. Bouzat. 2009. Single-channel kinetic analysis for activation and desensitization of homomeric 5-HT(3)A receptors. *Biophys. J.* 97:1335–1345. https://doi.org/10.1016/j.bpj.2009.06.018

Cuevas, J., A.L. Roth, and D.K. Berg. 2000. Two distinct classes of functional 7-containing nicotinic receptor on rat superior cervical ganglion neurons. *J. Physiol.* 525:735–746. https://doi.org/10.1111/j.1469-7793.2000.t01-1-00735.x

Descarries, L., V. Gisiger, and M. Steriade. 1997. Diffuse transmission by acetylcholine in the CNS. *Prog. Neurobiol.* 53:603–625. https://doi.org/10.1016/S0301-0082(97)00050-6

DeLano WL. "PyMOL." 700 (2002).
Deutsch, S.I., J.A. Burket, A.D. Benson, and M.R. Urbano. 2016. The 15q13.3 deletion syndrome: Deficient α(7)-containing nicotinic acetylcholine receptor-mediated neurotransmission in the pathogenesis of neurodevelopmental disorders. *Prog. Neuropsychopharmacol. Biol. Psychiatry*. 64:109–117. https://doi.org/10.1016/j.pnpbp.2015.08.001
Dineley, K.T., A.A. Pandya, and J.L. Yakel. 2015. Nicotinic ACh receptors as therapeutic targets in CNS disorders. *Trends Pharmacol. Sci*. 36:96–108. https://doi.org/10.1016/j.tips.2014.12.002
Dolinsky, T.J., P. Czodrowski, H. Li, J.E. Nielsen, J.H. Jensen, G. Klebe, and N.A. Baker. 2007. PDB2PQR: expanding and upgrading automated preparation of biomolecular structures for molecular simulations. *Nucleic Acids Res*. 35. W522-5. https://doi.org/10.1093/nar/gkm276
Drisdel, R.C., and W.N. Green. 2000. Neuronal alpha-bungarotoxin receptors are alpha7 subunit homomers. *J. Neurosci*. 20:133–139. https://doi.org/10.1523/JNEUROSCI.20-01-00133.2000
Du, J., W. Lü, S. Wu, Y. Cheng, and E. Gouaux. 2015. Glycine receptor mechanism elucidated by electron cryo-microscopy. *Nature*. 526:224–229. https://doi.org/10.1038/nature14853
Duffy, A.M., P. Zhou, T.A. Milner, and V.M. Pickel. 2009. Spatial and intracellular relationships between the α7 nicotinic acetylcholine receptor and the vesicular acetylcholine transporter in the prefrontal cortex of rat and mouse. *Neuroscience*. 161:1091–1103. https://doi.org/10.1016/j.neuroscience.2009.04.024
Egelman, D.M., and P.R. Montague. 1999. Calcium dynamics in the extracellular space of mammalian neural tissue. *Biophys. J*. 76:1856–1867. https://doi.org/10.1016/S0006-3495(99)77345-5
Eiselé, J.L., S. Bertrand, J.L. Galzi, A. Devillers-Thiéry, J.P. Changeux, and D. Bertrand. 1993. Chimaeric nicotinic-serotonergic receptor combines distinct ligand binding and channel specificities. *Nature*. 366:479–483. https://doi.org/10.1038/366479a0
Essmann, U., L. Perera, and M.L. Berkowitz. 1995. Darden. T., Lee, H., Pedersen, L. G. A smooth particle mesh Ewald method. *J. Chem. Phys*. 103:8577–8593. https://doi.org/10.1063/1.470117
Fucile, S.. 2004. Ca^{2+} permeability of nicotinic acetylcholine receptors. *Cell Calcium*. 35:1–8. https://doi.org/10.1016/j.ceca.2003.08.006
Galzi, J.L., S. Bertrand, P.J. Corringer, J.P. Changeux, and D. Bertrand. 1996. Identification of calcium binding sites that regulate potentiation of a neuronal nicotinic acetylcholine receptor. *EMBO J*. 15:5824–5832. https://doi.org/10.1002/j.1460-2075.1996.tb00969.x
Gao, F., N. Bren, T.P. Burghardt, S. Hansen, R.H. Henchman, P. Taylor, J.A. McCammon, and S.M. Sine. 2005. Agonist-mediated conformational changes in acetylcholine-binding protein revealed by simulation and intrinsic tryptophan fluorescence. *J. Biol. Chem*. 280:8443–8451. https://doi.org/10.1074/jbc.M412389200
Gharpure, A., J. Teng, Y. Zhuang, C.M. Noviello, R.M. Walsh, Jr., R. Cabuco, R.J. Howard, N.T. Zaveri, E. Lindahl, and R.E. Hibbs. 2019. Agonist selectivity and ion permeation in the α3β4 ganglionic nicotinic receptor. *Neuron*. 104:501–511.e6: E6. https://doi.org/10.1016/j.neuron.2019.07.030
Grady, S.R., M. Moretti, M. Zoli, M.J. Marks, A. Zanardi, L. Pucci, F. Clementi, and C. Gotti. 2009. Rodent habenulo-interpeduncular pathway expresses a large variety of uncommon nAChR subtypes, but only the α3β4* and α3β3β4* subtypes mediate acetylcholine release. *J. Neurosci*. 29:2272–2282. https://doi.org/10.1523/JNEUROSCI.5121-08.2009
Greene, L.A., A.J. Sytkowski, Z. Vogel, and M.W. Nirenberg. 1973. -Bungarotoxin used as a probe for acetylcholine receptors of cultured neurones. *Nature*. 243:163–166. https://doi.org/10.1038/243163a0
Gu, S., J.A. Matta, B. Lord, A.W. Harrington, S.W. Sutton, W.B. Davini, and D.S. Bredt. 2016. Brain α7 Nicotinic Acetylcholine Receptor Assembly Requires NACHO. *Neuron*. 89:948–955. https://doi.org/10.1016/j.neuron.2016.01.018
Hamill, O.P., A. Marty, E. Neher, B. Sakmann, and F.J. Sigworth. 1981. Improved patch-clamp techniques for high-resolution current recording from cells and cell-free membrane patches. *Pflugers Arch*. 391:85–100. https://doi.org/10.1007/BF00656997
Hansen, S.B., G. Sulzenbacher, T. Huxford, P. Marchot, P. Taylor, and Y. Bourne. 2005. Structures of Aplysia AChBP complexes with nicotinic agonists and antagonists reveal distinctive binding interfaces and conformations. *EMBO J*. 24:3635–3646. https://doi.org/10.1038/sj.emboj.7600828
Huang, J., S. Rauscher, G. Nawrocki, T. Ran, M. Feig, B.L. de Groot, H. Grubmüller, and A.D. MacKerell, Jr.. 2017. CHARMM36m: an improved force field for folded and intrinsically disordered proteins. *Nat. Methods*. 14:71–73. https://doi.org/10.1038/nmeth.4067
Inakollu, V.S., D.P. Geerke, C.N. Rowley, and H. Yu. 2020. Polarisable force fields: what do they add in biomolecular simulations? *Curr. Opin. Struct. Biol*. 61:182–190. https://doi.org/10.1016/j.sbi.2019.12.012
Jacob, M.H., and D.K. Berg. 1983. The ultrastructural localization of alpha-bungarotoxin binding sites in relation to synapses on chick ciliary ganglion neurons. *J. Neurosci*. 3:260–271. https://doi.org/10.1523/JNEUROSCI.03-02-00260.1983
Jones, I.W., and S. Wonnacott. 2004. Precise localization of α7 nicotinic acetylcholine receptors on glutamatergic axon terminals in the rat ventral tegmental area. *J. Neurosci*. 24:11244–11252. https://doi.org/10.1523/JNEUROSCI.3009-04.2004
Kaczanowska, K., M. Harel, Z. Radić, J.P. Changeux, M.G. Finn, and P. Taylor. 2014. Structural basis for cooperative interactions of substituted 2-aminopyrimidines with the acetylcholine binding protein. *Proc. Natl. Acad. Sci. USA*. 111:10749–10754. https://doi.org/10.1073/pnas.1410992111
Lee, W.Y., and S.M. Sine. 2005. Principal pathway coupling agonist binding to channel gating in nicotinic receptors. *Nature*. 438:243–247. https://doi.org/10.1038/nature04156
Lee, B.S., R.B. Gunn, and R.R. Kopito. 1991. Functional differences among nonerythroid anion exchangers expressed in a transfected human cell line. *J. Biol. Chem*. 266:11448–11454.
Leiser, S.C., M.R. Bowlby, T.A. Comery, and J. Dunlop. 2009. A cog in cognition: how the α 7 nicotinic acetylcholine receptor is geared towards improving cognitive deficits. *Pharmacol. Ther*. 122:302–311. https://doi.org/10.1016/j.pharmthera.2009.03.009
Lendvai, B., and E.S. Vizi. 2008. Nonsynaptic chemical transmission through nicotinic acetylcholine receptors. *Physiol. Rev*. 88:333–349. https://doi.org/10.1152/physrev.00040.2006
Li, S.X., S. Huang, N. Bren, K. Noridomi, C.D. Dellisanti, S.M. Sine, and L. Chen. 2011. Ligand-binding domain of an α7-nicotinic receptor chimera and its complex with agonist. *Nat. Neurosci*. 14:1253–1259. https://doi.org/10.1038/nn.2908
Liu, Y., and J.P. Dilger. 1991. Opening rate of acetylcholine receptor channels. *Biophys. J*. 60:424–432. https://doi.org/10.1016/S0006-3495(91)82068-9
Mansvelder, H.D., and D.S. McGehee. 2000. Long-term potentiation of excitatory inputs to brain reward areas by nicotine. *Neuron*. 27:349–357. https://doi.org/10.1016/S0896-6273(00)00042-8
Masiulis, S., R. Desai, T. Uchański, I. Serna Martin, D. Laverty, D. Karia, T. Malinauskas, J. Zivanov, E. Pardon, A. Kotecha, et al. 2019. $GABA_A$ receptor signalling mechanisms revealed by structural pharmacology. *Nature*. 565:454–459. https://doi.org/10.1038/s41586-018-0832-5
McLaughlin, J.T., J. Fu, A.D. Sproul, and R.L. Rosenberg. 2006. Role of the outer β-sheet in divalent cation modulation of α7 nicotinic receptors. *Mol. Pharmacol*. 70:16–22. https://doi.org/10.1124/mol.106.023259
Mukhtasimova, N., and S.M. Sine. 2013. Nicotinic receptor transduction zone: invariant arginine couples to multiple electron-rich residues. *Biophys. J*. 104:355–367. https://doi.org/10.1016/j.bpj.2012.12.013
Mukhtasimova, N., C.J.B. daCosta, and S.M. Sine. 2016. Improved resolution of single channel dwell times reveals mechanisms of binding, priming, and gating in muscle AChR. *J. Gen. Physiol*. 148:43–63. https://doi.org/10.1085/jgp.201611584
Mulle, C., C. Léna, and J.P. Changeux. 1992. Potentiation of nicotinic receptor response by external calcium in rat central neurons. *Neuron*. 8:937–945. https://doi.org/10.1016/0896-6273(92)90208-U
Nicholson, C., G.T. Bruggencate, R. Steinberg, and H. Stöckle. 1977. Calcium modulation in brain extracellular microenvironment demonstrated with ion-selective micropipette. *Proc. Natl. Acad. Sci. USA*. 74:1287–1290. https://doi.org/10.1073/pnas.74.3.1287
Pear, W.S., G.P. Nolan, M.L. Scott, and D. Baltimore. 1993. Production of high-titer helper-free retroviruses by transient transfection. *Proc. Natl. Acad. Sci. USA*. 90:8392–8396. https://doi.org/10.1073/pnas.90.18.8392
Phillips, J.C., R. Braun, W. Wang, J. Gumbart, E. Tajkhorshid, E. Villa, C. Chipot, R.D. Skeel, L. Kalé, and K. Schulten. 2005. Scalable molecular dynamics with NAMD. *J. Comput. Chem*. 26:1781–1802. https://doi.org/10.1002/jcc.20289
Plummer, H.K., III, M. Dhar, and H.M. Schuller. 2005. Expression of the α7 nicotinic acetylcholine receptor in human lung cells. *Respir. Res*. 6:29. https://doi.org/10.1186/1465-9921-6-29
Pumain, R., I. Kurcewicz, and J. Louvel. 1983. Fast extracellular calcium transients: involvement in epileptic processes. *Science*. 222:177–179. https://doi.org/10.1126/science.6623068
Qin, F., A. Auerbach, and F. Sachs. 1996. Estimating single-channel kinetic parameters from idealized patch-clamp data containing missed events. *Biophys. J*. 70:264–280. https://doi.org/10.1016/S0006-3495(96)79568-1

Quick, M.W., R.M. Ceballos, M. Kasten, J.M. McIntosh, and R.A. Lester. 1999. Alpha3beta4 subunit-containing nicotinic receptors dominate function in rat medial habenula neurons. *Neuropharmacology*. 38:769–783. https://doi.org/10.1016/S0028-3908(99)00024-6

Rahman, M.M., J. Teng, B.T. Worrell, C.M. Noviello, M. Lee, A. Karlin, M.H.B. Stowell, and R.E. Hibbs. 2020. Structure of the native muscle-type nicotinic receptor and inhibition by snake venom toxins. *Neuron*. 106: 952–962.e5. https://doi.org/10.1016/j.neuron.2020.03.012

Rusakov, D.A., and A. Fine. 2003. Extracellular Ca^{2+} depletion contributes to fast activity-dependent modulation of synaptic transmission in the brain. *Neuron*. 37:287–297. https://doi.org/10.1016/S0896-6273(03)00025-4

Ryckaert, J.P., G. Ciccotti, and H.J.C. Berendsen. 1997. Numerical integration of the cartesian equations of motion of a system with constraints: molecular dynamics of n-alkanes. *J. Comput. Phys*. 23:327–341. https://doi.org/10.1016/0021-9991(77)90098-5

Sarter, M., V. Parikh, and W.M. Howe. 2009. Phasic acetylcholine release and the volume transmission hypothesis: time to move on. *Nat. Rev. Neurosci*. 10:383–390. https://doi.org/10.1038/nrn2635

Sauguet, L., A. Shahsavar, F. Poitevin, C. Huon, A. Menny, À. Nemecz, A. Haouz, J.P. Changeux, P.J. Corringer, and M. Delarue. 2014. Crystal structures of a pentameric ligand-gated ion channel provide a mechanism for activation. *Proc. Natl. Acad. Sci. USA*. 111:966–971. https://doi.org/10.1073/pnas.1314997111

Schoepfer, R., W.G. Conroy, P. Whiting, M. Gore, and J. Lindstrom. 1990. Brain alpha-bungarotoxin binding protein cDNAs and MAbs reveal subtypes of this branch of the ligand-gated ion channel gene superfamily. *Neuron*. 5:35–48. https://doi.org/10.1016/0896-6273(90)90031-A

Séguéla, P., J. Wadiche, K. Dineley-Miller, J.A. Dani, and J.W. Patrick. 1993. Molecular cloning, functional properties, and distribution of rat brain α7: a nicotinic cation channel highly permeable to calcium. *J. Neurosci*. 13: 596–604. https://doi.org/10.1523/JNEUROSCI.13-02-00596.1993

Sharma, G., and S. Vijayaraghavan. 2001. Nicotinic cholinergic signaling in hippocampal astrocytes involves calcium-induced calcium release from intracellular stores. *Proc. Natl. Acad. Sci. USA*. 98:4148–4153. https://doi.org/10.1073/pnas.071540198

Shytle, R.D., T. Mori, K. Townsend, M. Vendrame, N. Sun, J. Zeng, J. Ehrhart, A.A. Silver, P.R. Sanberg, and J. Tan. 2004. Cholinergic modulation of microglial activation by alpha 7 nicotinic receptors. *J. Neurochem*. 89: 337–343. https://doi.org/10.1046/j.1471-4159.2004.02347.x

Sigworth, F.J., and S.M. Sine. 1987. Data transformations for improved display and fitting of single-channel dwell time histograms. *Biophys. J*. 52: 1047–1054. https://doi.org/10.1016/S0006-3495(87)83298-8

Silver, I.A., and M. Erecińska. 1990. Intracellular and extracellular changes of [Ca2+] in hypoxia and ischemia in rat brain in vivo. *J. Gen. Physiol*. 95: 837–866. https://doi.org/10.1085/jgp.95.5.837

Sine, S.M., J.R. Strikwerda, and S. Mazzaferro. 2019. Structural basis for α-bungarotoxin insensitivity of neuronal nicotinic acetylcholine receptors. *Neuropharmacology*. 160. 107660.

Suresh, A., and A. Hung. 2019. Structural effects of divalent calcium cations on the α7 nicotinic acetylcholine receptor: A molecular dynamics simulation study. *Proteins*. 87:992–1005. https://doi.org/10.1002/prot.25761

Vernino, S., M. Amador, C.W. Luetje, J. Patrick, and J.A. Dani. 1992. Calcium modulation and high calcium permeability of neuronal nicotinic acetylcholine receptors. *Neuron*. 8:127–134. https://doi.org/10.1016/0896-6273(92)90114-S

Walsh, R.M., Jr., S.H. Roh, A. Gharpure, C.L. Morales-Perez, J. Teng, and R.E. Hibbs. 2018. Structural principles of distinct assemblies of the human α4β2 nicotinic receptor. *Nature*. 557:261–265. https://doi.org/10.1038/s41586-018-0081-7

Wang, H., M. Yu, M. Ochani, C.A. Amella, M. Tanovic, S. Susarla, J.H. Li, H. Wang, H. Yang, L. Ulloa, et al. 2003. Nicotinic acetylcholine receptor alpha7 subunit is an essential regulator of inflammation. *Nature*. 421: 384–388. https://doi.org/10.1038/nature01339

Williams, N.M., B. Franke, E. Mick, R.J. Anney, C.M. Freitag, M. Gill, A. Thapar, M.C. O'Donovan, M.J. Owen, P. Holmans, et al. 2012. Genome-wide analysis of copy number variants in attention deficit hyperactivity disorder: the role of rare variants and duplications at 15q13.3. *Am. J. Psychiatry*. 169:195–204. https://doi.org/10.1176/appi.ajp.2011.11060822

Yang, Y., C.D. Paspalas, L.E. Jin, M.R. Picciotto, A.F.T. Arnsten, and M. Wang. 2013. Nicotinic α7 receptors enhance NMDA cognitive circuits in dorsolateral prefrontal cortex. *Proc. Natl. Acad. Sci. USA*. 110:12078–12083. https://doi.org/10.1073/pnas.1307849110

Zhang, A., H. Yu, C. Liu, and C. Song. 2020. The Ca^{2+} permeation mechanism of the ryanodine receptor revealed by a multi-site ion model. *Nat. Commun*. 11:922. https://doi.org/10.1038/s41467-020-14573-w

Supplemental material

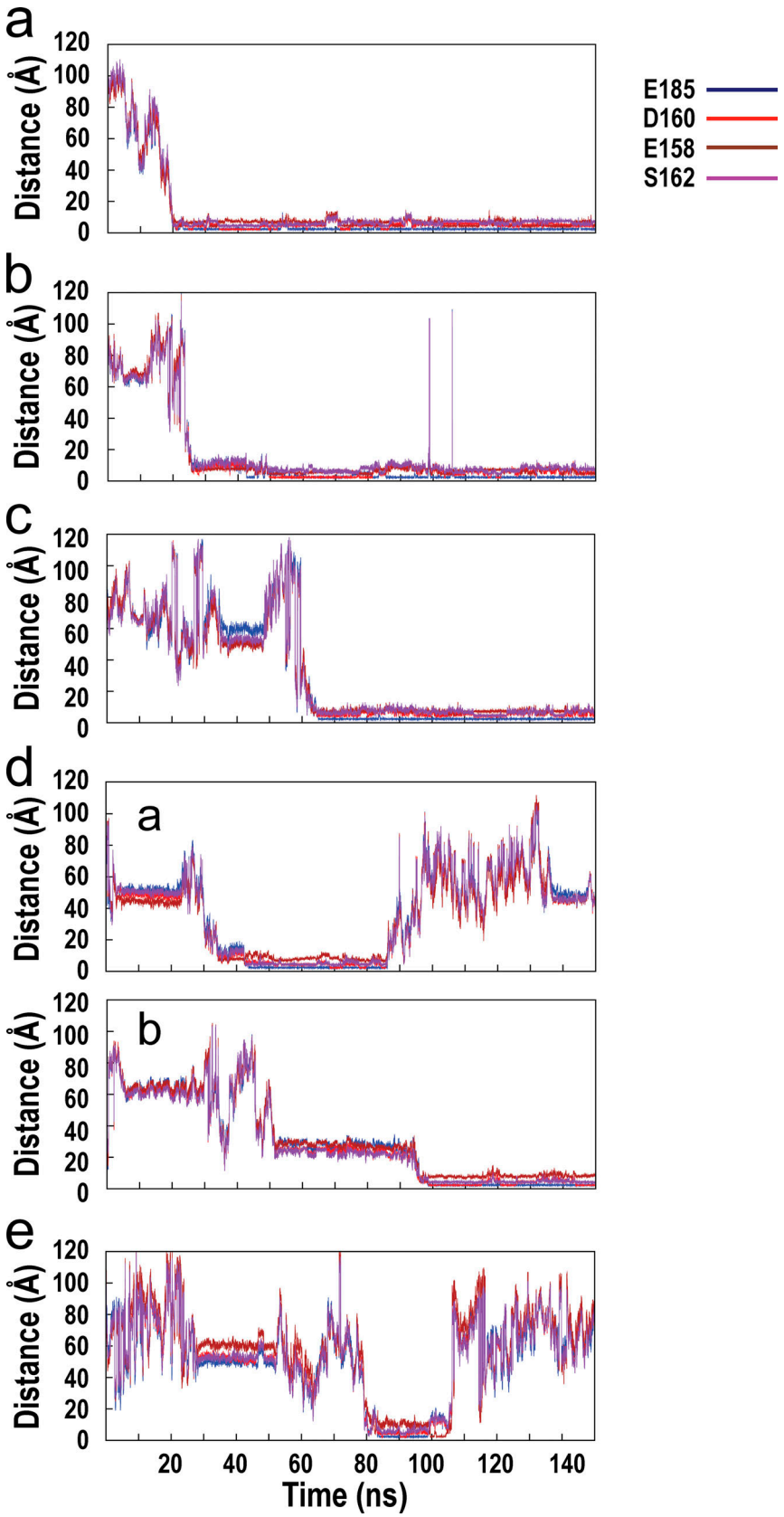

Figure S1. **Time evolution of the interatomic distances between the associating calcium ion and the oxygen atoms of key stabilizing residues from the C-loop and F-loop of the wild-type α7/AChBP during the course of MD simulation. (a–e)** Results for four associating calcium ions are shown, while results for the fifth calcium ion are shown in Fig. 4 d of the main text. **(d)** For one of the binding sites, two trajectories are shown, one for the first calcium that binds and then dissociates (a) and the other for the second calcium that binds shortly after the first calcium dissociates (b).

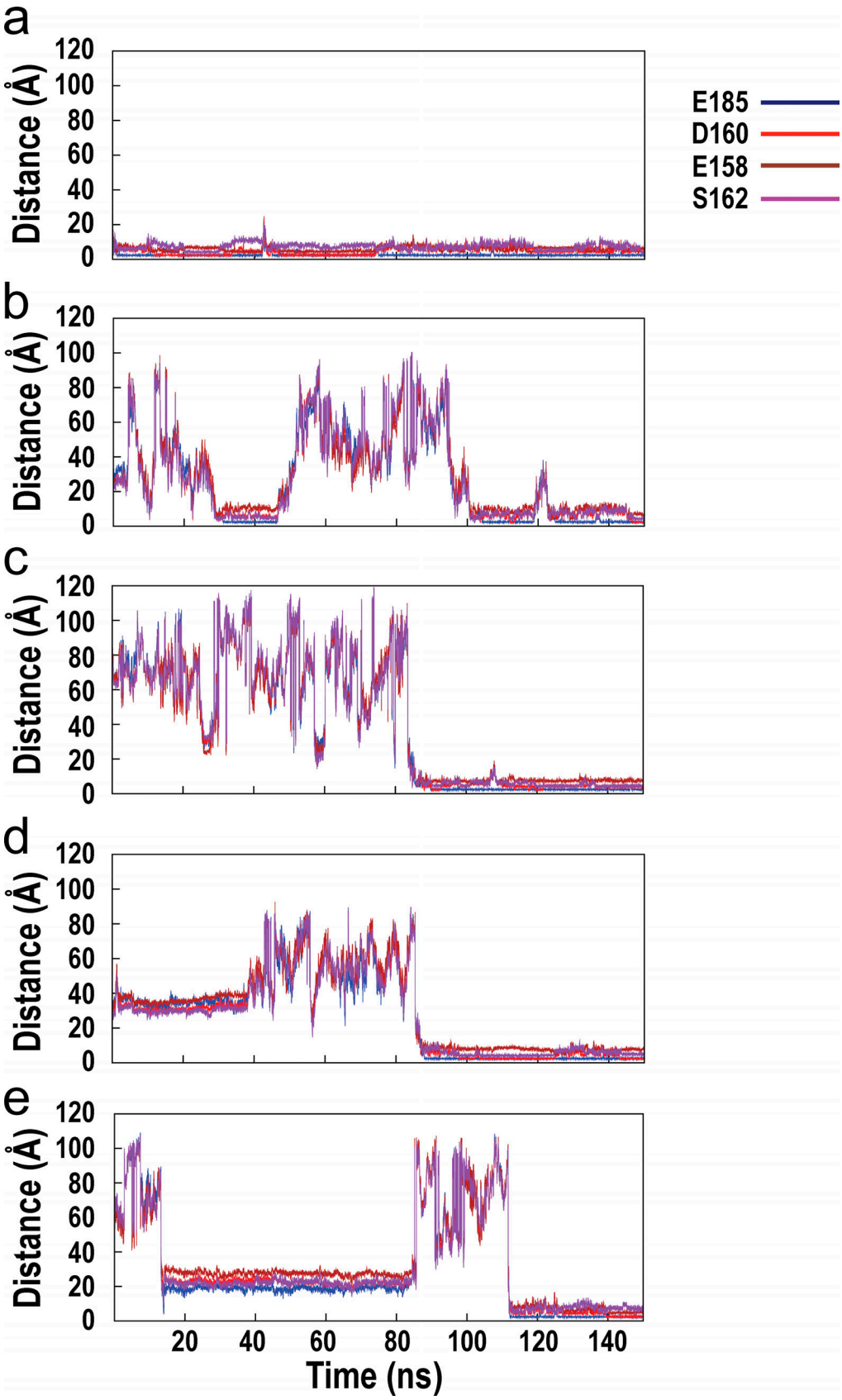

Figure S2. **Time evolution of the interatomic distances between the associating calcium ion and the oxygen atoms of key stabilizing residues from the C-loop and F-loop of the E158A mutant of α7/AChBP during the course of MD simulation. (a–e)** Results for all five associating calcium ions are shown.

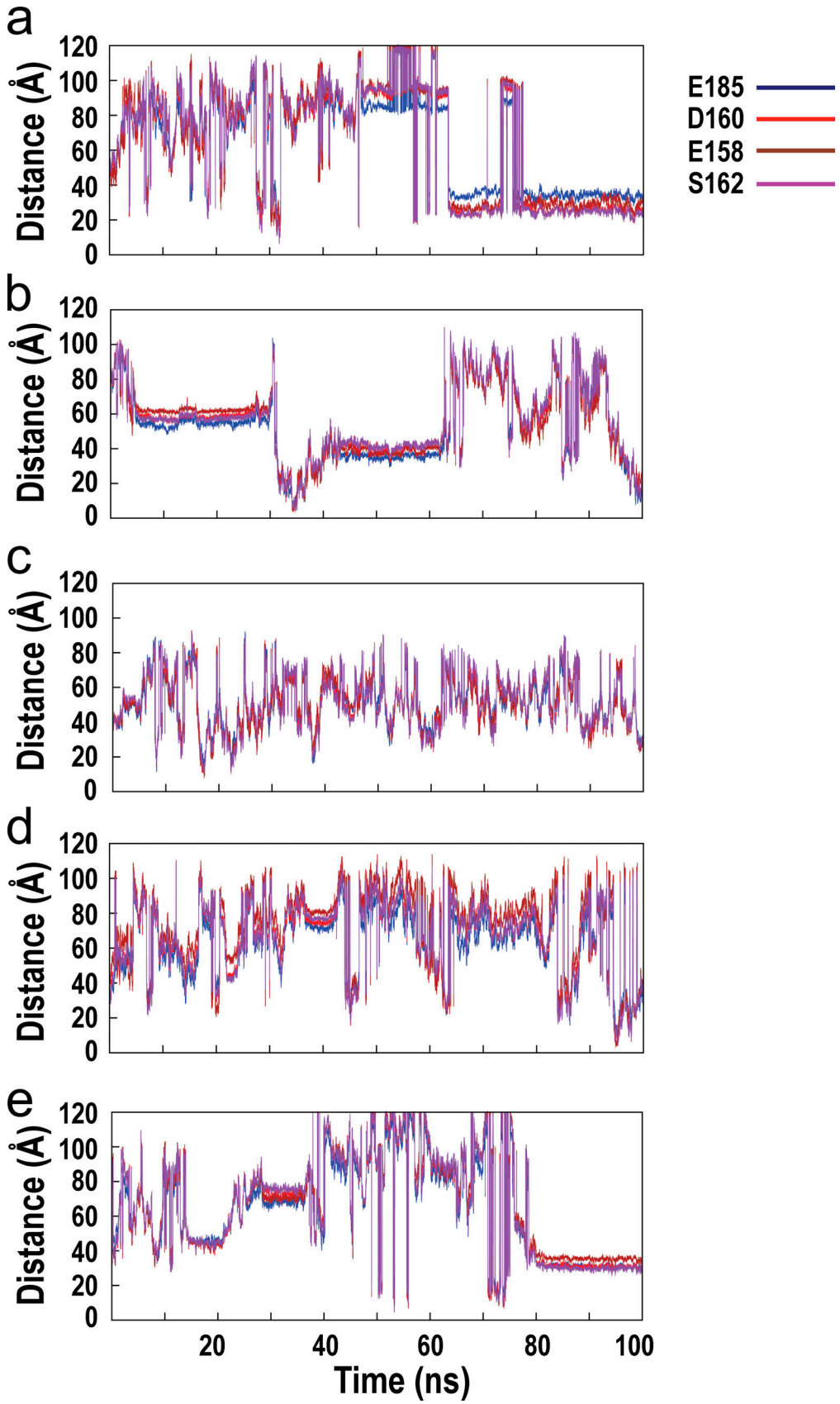

Figure S3. **Time evolution of the interatomic distances between the associating calcium ion and the oxygen atoms of key stabilizing residues from the C-loop and F-loop of the E185Q mutant of α7/AChBP during the course of MD simulation. (a–e)** Results for all five associating calcium ions are shown.

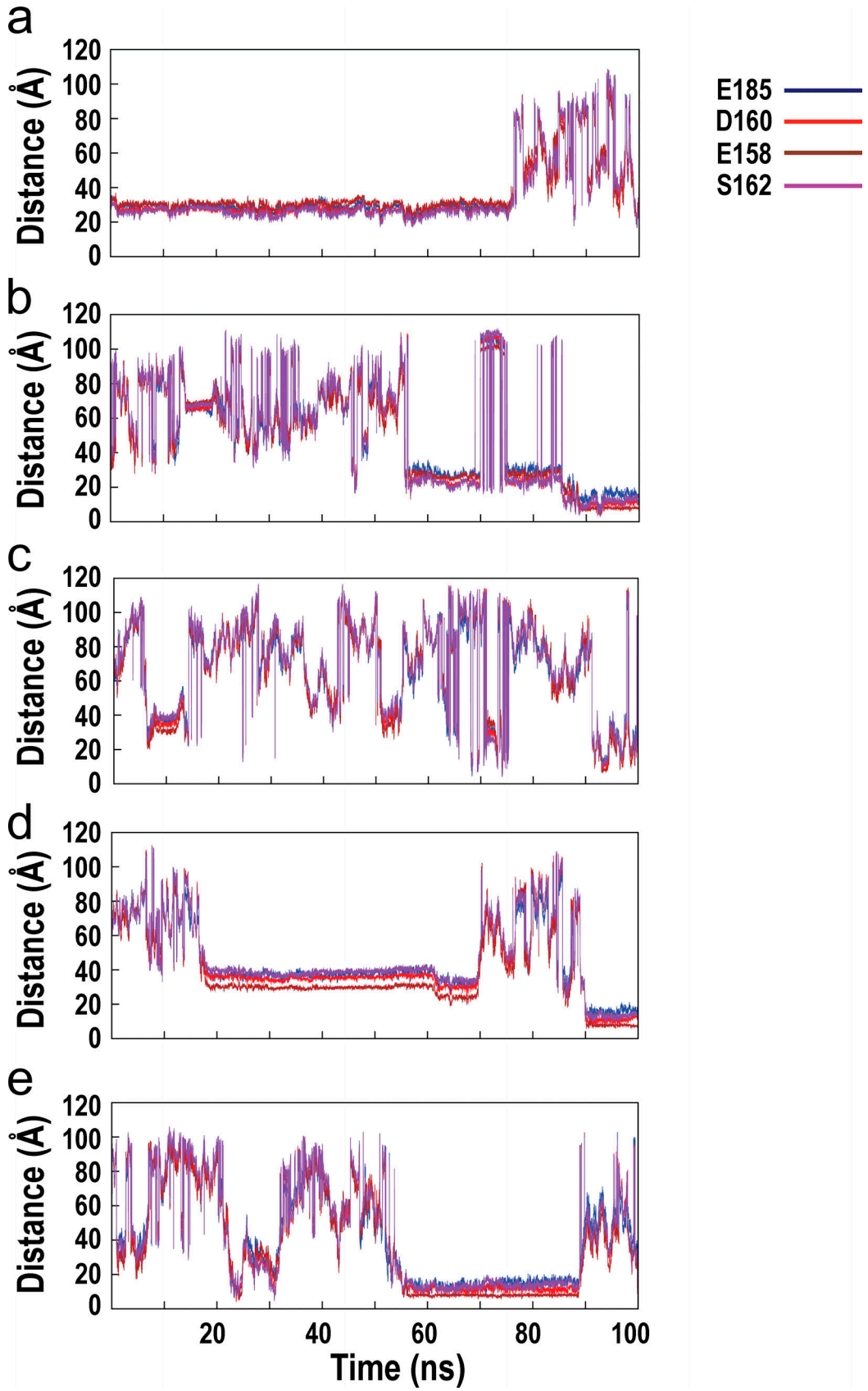

Figure S4. **Time evolution of the interatomic distances between the associating calcium ion and the oxygen atoms of key stabilizing residues from the C-loop and F-loop of the D160S mutant of α7/AChBP during the course of MD simulation. (a–e)** Results for all five associating calcium ions are shown.